核理研研究報告　第40巻　2007年

ISSN 0385-2105

RESEARCH REPORT OF LABORATORY OF NUCLEAR SCIENCE

Vol.40　2007

TOHOKU UNIVERSITY

Editors

TAMAE, Tadaaki

OHTSUKI, Tsutomu

HAMA, Hiroyuki

Laboratory of Nuclear Science

Tohoku University

1-2-1 Mikamine, Taihaku, Sendai 982-0826

Japan

Pone: +81, 22-743-3400

Fax: +81, 22-743-3401

Web site: http://www.lns.tohoku.ac.jp/

982-0826 仙台市太白区三神峯1-2-1

東北大学大学院理学研究科

附属原子核理学研究施設

電話　022-743-3400

Fax　022-743-3401

Preface

This issue of Research Report of Laboratory of Nuclear Science reports research activities of the LNS performed in the 2006 academic/fiscal year (April 2006 – March 2007). Major research activities are based on the electron accelerator complex consisting of the 300-MeV LINAC and the 1.2-GeV STB ring. The accelerators have altogether provided a beam time of about 2,380 hours for various experiments through the year.

In the GeV-γ experimental hall, construction of a 4π spectrometer called FOREST, which is an electro-magnetic calorimeter for neutral meson detection, has started. At this occasion, a beam line for counter test experiments was developed to provide low-intensity electron/positron beams with a momentum range from 200 to 800 MeV. In the experimental hall 2, commissioning of the New NKS spectrometer has essentially finished and the D(γ ,K^0) experiments for neutral Λ particle production has started in June. Various radioactive isotopes were produced by using high intensity beams below 50 MeV at the experimental hall 1. They were served for element analyses as well as for detailed study of decay properties of nuclei: the highlight is the change of positron capture rate in carbon fullerene.

We hope that this Report will serve as a quick overview of the present LNS activities over a variety of nuclear research fields.

Jirohta KASAGI
Director

Research Report of Laboratory of Nuclear Science
Volume 40, 2007

Contents

核理研研究報告　第40巻　目　次

Ⅰ．原子核物理

Ⅰ. Nuclear Physics

(LNS Experiment : #2552, #2565)

Study of Neutral Kaon Photo-Production at LNS-Tohoku

P. Bydžovský[1], N. Chiga [2], Y. Fujii [2], K. Futatsukawa[2], Y.C. Han [6], O. Hashimoto [2], K. Hirose [4], K. Hosomi [2], A. Iguchi [2], T. Ishikawa [4], H. Kanda [2], M. Kaneta [2], M. Kawai [2], T. Kawasaki [2], D. Kawama [2], S. Kiyokawa [2], T. Koike [2], O. Konno [5], Y. Ma [2], K. Maeda [2], N. Maruyama [2], A. Matsumura [2], M. Mimori [2], K. Miwa [2], Y. Miyagi [2], S.N. Nakamura [2], T. Ohtani [2], Y. Okayasu [2], A. Sasaki [3], H. Shimizu [4], K. Shirotori [2], M. Sotona [1], K. Suzuki [4], T. Tamae [4], H. Tamura [2], N. Terada [2], K. Tsukada [2], T.S. Wang [6], T. Yamamoto [2], H. Yamazaki [4], and K. Yokota [2]

[1]*Nuclear Physics Institute, 25068, Řež, Czech Republic*
[2]*Department of Physics, Tohoku University, Sendai 980-8578*
[3]*Department of Electrical and Electronic Engineering, Akita University, Akita 010-8502*
[4]*Laboratory of Nuclear Science, Tohoku University, Sendai 982-0826*
[5]*Department of Electrical Engineering, Ichinoseki National College of Technology, Ichinoseki 021-8511*
[6]*School of Nuclear Science and Technology, Lanzhou University, Tianshuinan Road 222, Lanzhou 730000, China*

§1. Introduction

The investigation of the kaon production on a nucleon by the electromagnetic interaction provides invaluable information on the strangeness production mechanism, strength of meson-baryon coupling constants and structure of hadrons, being labeled by the strangeness degree of freedom. Such studies using beams of real photons and electrons have been conducted experimentally and theoretically since the 1950's, taking advantage of the electromagnetic interaction that is understood better than the hadronic interaction. Until now, the experimental studies have been carried out in $p(\gamma, K^+)\Lambda$, $p(\gamma, K^+)\Sigma^0$ and $p(\gamma, K^0)\Sigma^+$ reactions among six isospin channels ([1], [2]). However, there are no data for the other three channels on a neutron. Theoretically, phenomenological models have been constructed based on measured channels so far. The isobar models, Kaon-MAID [3] and SLA [4], were adopted in the present analysis. The predictions of the photon energy dependence and the kaon angular distribution of the other three channels on a neutron using these models are quite different.

The lack of the key data for strangeness photoproduction of the three channels on a neutron is due to the experimental difficulties to measure neutral kaons and to prepare a neutron target. The measurement of these three strangeness production channels provides much information on the strangeness photoproduction mechanism. In particular, the $n(\gamma, K^0)\Lambda$ reaction has following features. (1) Since no charge is involved, the t-channel Born term does not contribute. (2) It is a mirror reaction to $p(\gamma, K^+)\Lambda$. For the hyperon resonance exchange terms, a coupling constant, $g_{K\Sigma N}$, changes its sign from the

isospin symmetry, $g_{K^0\Sigma^0 n} = -g_{K^+\Sigma^0 p}$, resulting the different interference effect. Furthermore, the number of resonances to be considered is small in the threshold region. Therefore, the $n(\gamma, K^0)\Lambda$ reaction is expected to play an essential role to investigate the strangeness photoproduction mechanism.

We have already taken exploratory data quite successfully with use of Neutral Kaon Spectrometer (NKS) at LNS-Tohoku in 2003 and 2004. We intend to extend the previous experiment by considerably upgrading the original neutral kaon spectrometer to a completely new neutral kaon spectrometer (NKS2), fully replacing the spectrometer magnet, tracking detectors and all the trigger counters. The new spectrometer NKS2 has significantly larger acceptance for neutral kaons compared with NKS, particularly covering forward angles and much better invariant mass resolution. The estimated acceptance of NKS2 is about 3 to 4 times (depend on momentum and model) larger for K^0_S than that of NKS. Additionally, it is about 8 to 10 times larger for Lambda. With this advantage, we expect simultaneous measurements of K^0_S and Λ. Additionally, we plan to measure other strangeness production channels and also Λ hyperon polarization in $\gamma + n$ and $\gamma + p$ reactions.

In this report, we present a status of NKS2 experiment. The NKS results are found in elsewhere [5, 6].

§2. The NKS2 Experiment

The NKS2 spectrometer is located the BM4 beam line of the second experimental hall of Laboratory of Nuclear Science (LNS), Tohoku University (see Fig. 1). The incident beam from LINAC has 0.2 GeV of the beam energy and is accelerated up to 1.2 GeV in Stretcher-Booster (STB) Ring. The photon beam is created as bremsstrahlung of electron by a carbon wire at STB Tagger system of Bending Magnet 4 (BM4). There is a dipole magnet which is called the sweep magnet for e^+e^- from photon conversion. The sweep magnet is the same one which is used in the previous experiment NKS.

The spectrometer is placed following the sweep magnet. The main magnet is a dipole which is renovated from a cyclotron magnet of Cyclotron RI center of Tohoku University (it is so called 680 magnet). Detectors of NKS2 are: Inner Hodoscope (IH), Straw Drift Chamber (SDC), Cylindrical Drift Chamber (CDC), Outer Hodoscope (OH), and Electron Veto counter (EV). Figure 2 shows detector position and 3D views are shown in Figs. 3 and 4. The detail description of the beam line and the spectrometer will be shown in the following sections.

§3. Results of the NKS2 experiment

The data taking for commissioning runs was carried out in Jan. Mar, Jun., and Sep. 2006 using the carbon target. During those runs, we had studied detector performance, data acquisition system, and trigger rate. The data taking using NKS2 was done in Nov. and Dec. 2006, and Jan. and Jun. 2007.

A preliminary invariant mass distribution of $\pi^+\pi^-$ pairs in $0.8 < E_\gamma < 1.1$ GeV is shown in Fig. 5. The number of tagged photons for the distribution was 3.2×10^{11} from 2006's runs.

The events that have two tracks and more was selected. The particle identification was done on 2 dimensional cut on TOF and momentum. After positive and negative pions was identified in the same

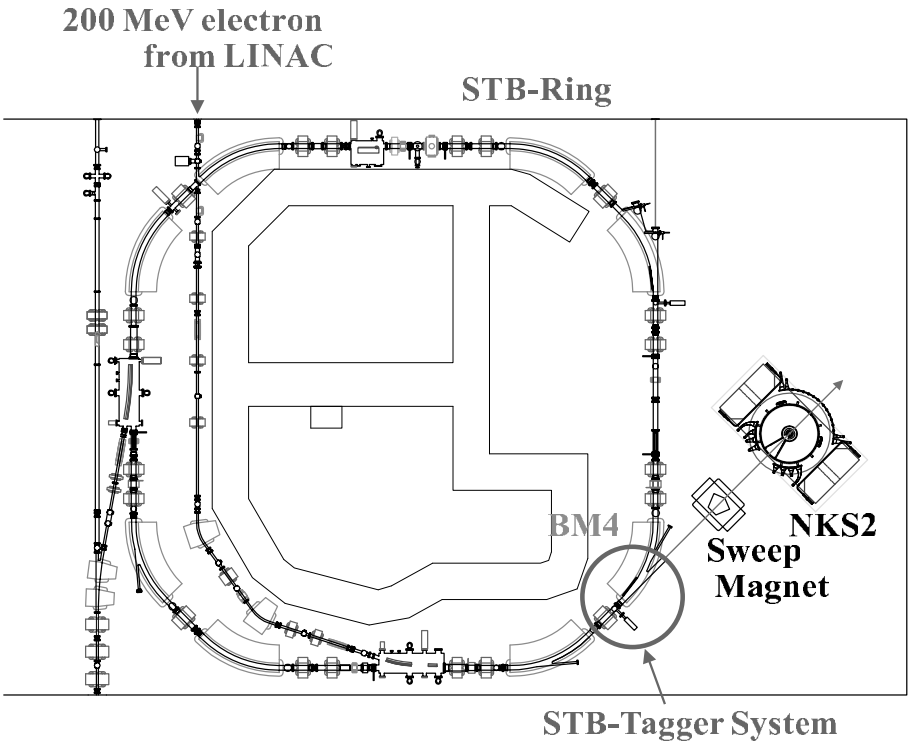

Fig.1. The outline of the second experimental hall of LNS (see text in detail).

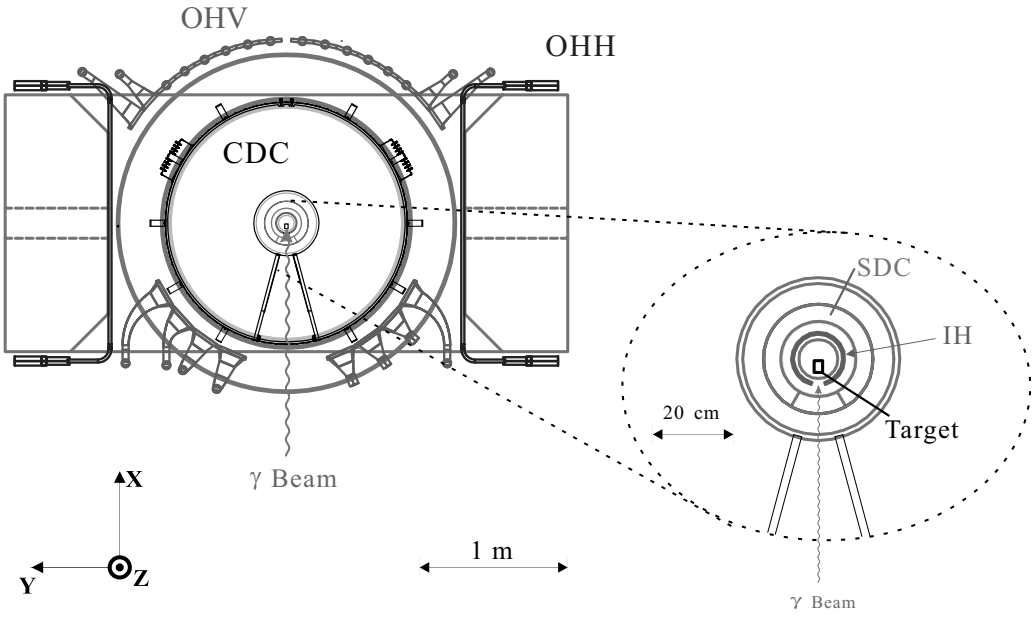

Fig.2. A schematic view of NKS2. The photon beam direction is bottom to top in the figure. The target holder is at center of magnet. The detectors are (the order is center to outer): Inner Hodoscope (IH), Straw Drift Chamber (SDC), Cylindrical Drift Chamber (CDC), Outer Hodoscope (OH, Vertical (OHV) and Horizontal (OHH)), and Electron Veto counter (EV). Note that EV is placed at downstream of OHV but not shown the figure.

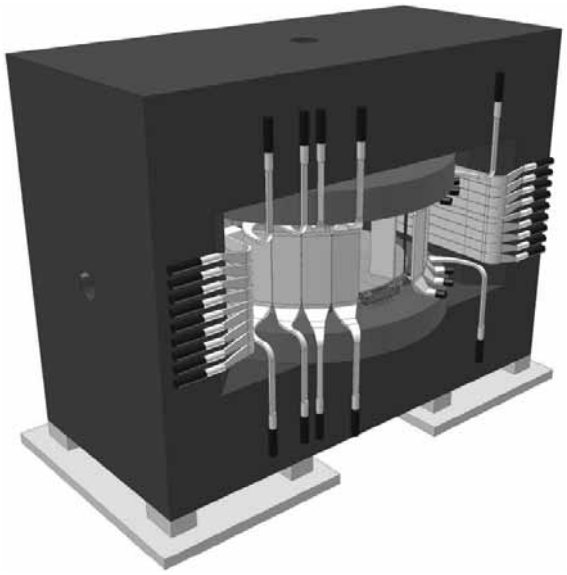

Fig.3. A 3D view of the spectrometer viewed from upstream of beam line. We can see a part of OHH on the magnet yoke and OHV around magnet coil.

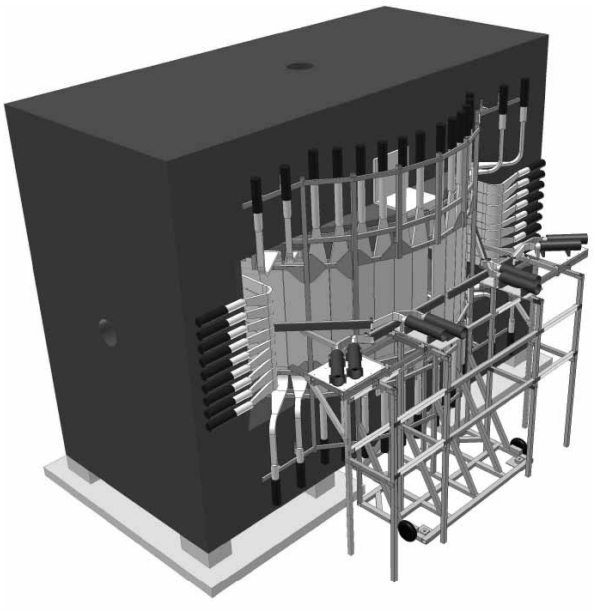

Fig.4. A 3D view of the spectrometer viewed from downstream of beam line. There are OHV around the magnet coil and OHH on the magnet yoke. The EV counters are placed following OHV. The OHV and EV counters are supported by aluminum chassis.

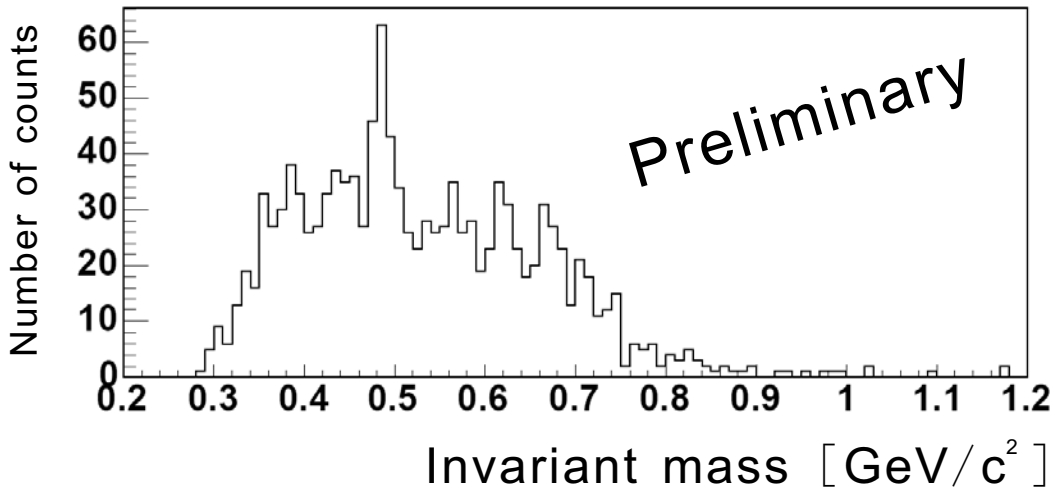

Fig.5. The invariant mass distribution of $\pi^+\pi^-$ pairs in $0.8 < E_\gamma < 1.1$ GeV.

event, the decay vertex was reconstructed from the two tracks. We required $-0.9 < \cos\theta_{OA} < 0.8$ (where θ_{OA} is an opening angle of two tracks) to select K^0_S candidate. We required an opening angle cut of two tracks to remove e^+e^- background. A decay volume cut was necessary to remove a background of resonances (e.g., ρ, ω). Since photoproduced vector mesons and nucleon resonances decay in the target region and create π^+ π^- background, we did not employ events which have their decay vertex position in the target cell. We employ events which have the decay vertex position at outside of the target cell to remove large contribution of hadronic background.

We have an upgrade plane of the spectrometer, that we will extend the acceptance by changing SDC with a 3D tracking chamber. With this advantage, we expect simultaneous measurements of K^0_S and Λ. Additionally, we plan to measure other strangeness production channels and also Λ hyperon polarization in $\gamma + n$ and $\gamma + p$ reactions.

Acknowledgement

This work is supported by Grant-In-Aid for Scientific Research from The Ministry of Education of Japan, Nos. 09304028, 12002001, 14740150 and 16GS0201.

References

[1] D.S. Caran *et al.*: Phys. Rev. Lett. **90** (2003) 131804.

[2] R.G.T. Zegers *et al.*: Phys. Rev. Lett. **91** (2003) 092001.

[3] F.X. Lee, T. Mart, C. Bennhold, and L.E. Wright: Nucl. Phys. **A695** (2001) 237.

[4] T. Mizutani, C. Fayard, G.H. Lamot, and B. Saghai: Phys. Rev. **C58** (1998) 75.

[5] T. Watanabe *et al.*: Phys. Lett. **B651** (2007) 269.

[6] K. Tsuakda *et al.*: arXiv:0712.0657(nucl-ex).

(LNS Experiment : #2563)

Electron/Positron Test Beamline

T. Ishikawa[1], R. Hashimoto[1], T. Ishida[1], J. Kasagi[1], S. Kuwasaki[1], K. Maeda[2], K. Mochizuki[1], K. Nawa[1], Y. Okada[1], Y. Onodera[1], H. Shimizu[1], K. Suzuki[1], and H. Yamazaki[1]

[1]*Laboratory of Nuclear Science, Tohoku University, Sendai, 982-0826*
[2]*Department of Physics, Tohoku University, Sendai, Miyagi 980-8578*

An electron/positron beamline for testing detectors has been constructed by utilizing a charge sweeping magnet $\mathcal{R}$TAGX, which can analyze the momentum of electrons and positrons at a fixed bending angle. The measured energy, profile, and intensity of the beam are reported together with a simulation result.

§1. Electron/Positron Beamline for Testing Detectors

A dipole electromagnet $\mathcal{R}$TAGX was installed two years ago [1] in the GeV-γ experimental hall, where meson production experiments have been conducted with an incident γ beam [2]. Besides sweeping out undesirable charged particles in the γ beam, the $\mathcal{R}$TAGX can provide momentum-analyzed electrons or positrons at a fixed bending angle. We have desired a beamline where performance tests can be made for many kinds of detectors. Thus an electron/positron beamline has been constructed in the GeV-γ experimental hall for testing detectors. The beamline consists of a converter, the $\mathcal{R}$TAGX magnet, and lead apertures as depicted in Fig.1. A Au foil, one of the converters, with a thickness of 20 μm is

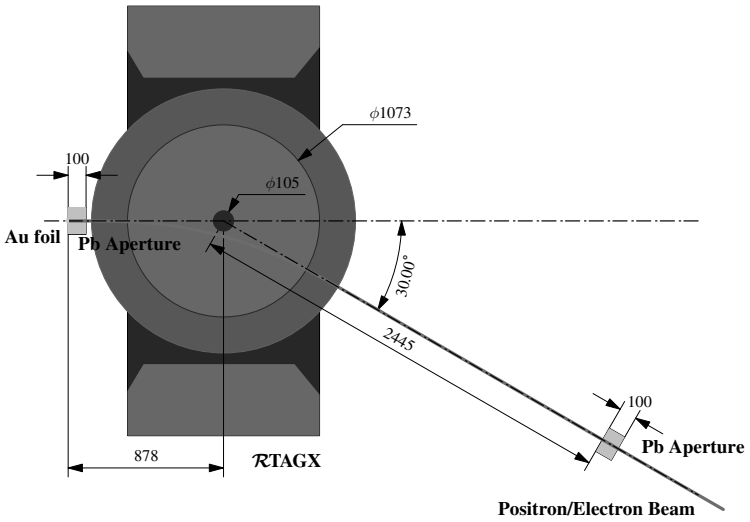

Fig.1. Schematic view of the electron/positron beamline for detector test. The beamline comprises a converter, a dipole electromagnet $\mathcal{R}$TAGX, and entrance and exit lead apertures. Electrons/positrons passing through the lead apertures are used as a beam.

placed 878 mm upstream of the pole center of the $\mathcal{R}$TAGX. There is a 100 mm thick lead aperture just behind the converter. Another 100 mm thick lead aperture with a diameter of 20 mm is placed 2445 mm downstream at -30° with respect to the axis of the incident γ beam. A vacuum chamber and a vacuum pipe were installed between two lead apertures on 23rd Apr. in 2007.

The incident γ beam coming into the GeV-γ experimental hall irradiates the converter in front of the $\mathcal{R}$TAGX. Some photons in the beam are converted into electron-positron pairs. The generated electrons and positrons are bent by the $\mathcal{R}$TAGX according to their momenta. Then semi-monochromatic electrons or positrons passing through the lead apertures are used as a beam.

§2. Estimated Energy and Resolution

The energy and resolution of the beam for a given $\mathcal{R}$TAGX current are estimated by a simulation code based on GEANT3 with a corresponding magnetic field map [1, 3]. Figure 2 shows the estimated beam energy as a function of the $\mathcal{R}$TAGX current and the energy resolution versus the beam energy.

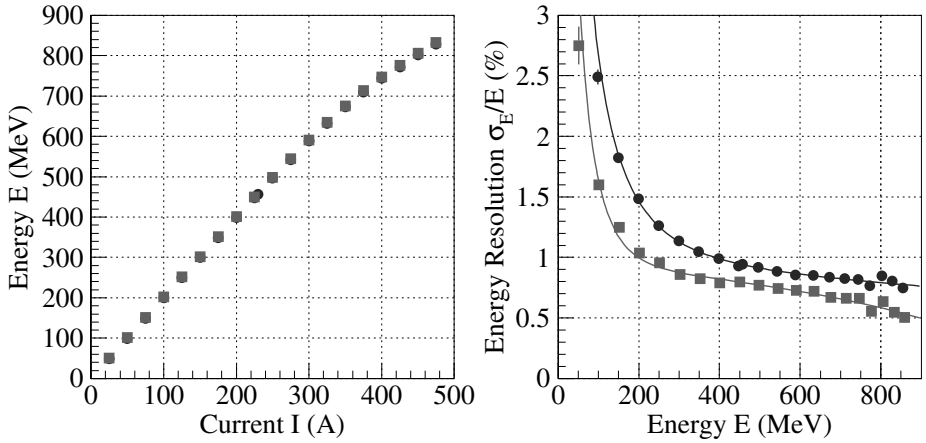

Fig.2. Estimated energy and resolution of the electron/positron beam with a simulation based on GEANT3. The left panel shows the mean energy as a function of $\mathcal{R}$TAGX current. The right panel shows the energy resolution as a function of the beam energy. The circle and square markers show the data points when the beam travels in the air and in the vacuum, respectively. Data points are fitted with the form $\sqrt{\boldsymbol{P}_1\boldsymbol{E}^{-2} + \boldsymbol{P}_2\boldsymbol{E}^{-1} + \boldsymbol{P}_3 + \boldsymbol{P}_4\boldsymbol{E}}$.

The electron/positron beam energy is almost proportional to the $\mathcal{R}$TAGX current. The value of the energy in MeV corresponds roughly to twice of that of the current in ampere. The energy resolution as a function of the energy is described as

$$\frac{\boldsymbol{\sigma_E}}{\boldsymbol{E}}(\boldsymbol{E}) = \sqrt{\frac{(7.49 \pm 0.26) \times 10^5}{\boldsymbol{E}^2} - \frac{(125.9 \pm 13.5)}{\boldsymbol{E}} + (0.977 \pm 0.028) - (3.9 \pm 0.2) \times 10^{-4}\boldsymbol{E}} \quad (1)$$

when electrons or positrons travel in the air, while that is described as

$$\frac{\boldsymbol{\sigma_E}}{\boldsymbol{E}}(\boldsymbol{E}) = \sqrt{\frac{(1.08 \pm 0.15) \times 10^5}{\boldsymbol{E}^2} - \frac{(8.6 \pm 78.1)}{\boldsymbol{E}} + (0.695 \pm 0.149) - (2.1 \pm 1.1) \times 10^{-4}\boldsymbol{E}} \quad (2)$$

when they travel in the vacuum. The numerical data are given in Ref. [4].

§3. Measured Beam Energy and Intensity

The beam energy was measured with a lead glass Čerenkov counter. The beam profile was also measured with a beam profile monitor (BPM). The BPM consists of two layers of scintillating fiber (SciFi) hodoscopes, each of which is made up with 16 SciFi modules. The fiber measures 3×3 mm^2 in cross section. The upstream and downstream layers determine x and y positions from responded fibers, respectively.

Figure 3 shows the measured energy distributions, and the beam profile for the $\mathcal{R}$TAGX current of 230 A. The measured energy is consistent with an estimated one, although the energy spread of the beam is not detectable because of poor energy-resolution of the lead glass counter. The size of the beam spot is about 50 mm in diameter at the place about 7 m from the center of the $\mathcal{R}$TAGX.

Figure 4 shows the beam intensity as a function of the $\mathcal{R}$TAGX current.

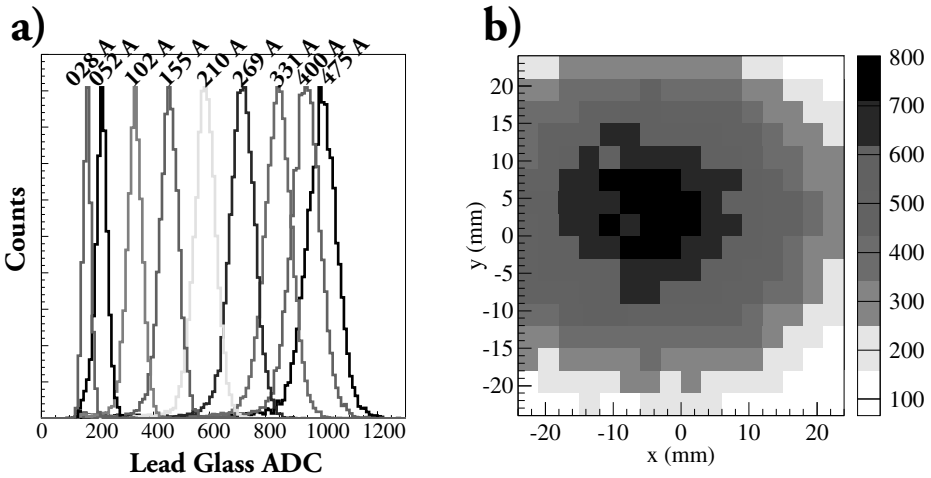

Fig.3. a) Measured beam energy distribution for several $\mathcal{R}$TAGX currents. The unit of energy is arbitrary (ADC channel). b) Measured beam profile for the $\mathcal{R}$TAGX current of 230 A. Both data were measured before the vacuum chamber had been installed.

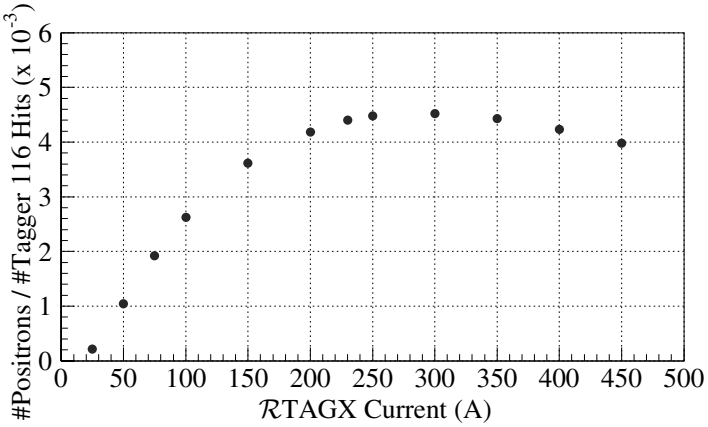

Fig.4. Intensity of the positron beam as a function of the $\mathcal{R}$TAGX current with a converter of 20 μm thick Au foil. The intensity is normalized by the counting rate of the 116th channel of the STB-Tagger II.

Since the beam intensity depends on the circulating electron current in the STretcher Booster ring, it is normalized by the counting rate of the 116th channel of the STB-Tagger II [5]. More intense beam can be obtained with a thicker converter. So far, the maximum intensity of the positron beam is about 700 kcps with an 8 mm thick Cu converter.

References

[1] T. Ishikawa *et al.*: Research Report of LNS, Tohoku University **39** (2006) 39.

[2] H. Shimizu *et al.*: Research Report of LNS, Tohoku University **37** (2004) 13.

[3] T. Ishikawa: Internal GeV-γ analysis notes Nos. **20** and **34** (2006).

[4] T. Ishikawa: Internal GeV-γ analysis note No. **43** (2007).

[5] T. Nakabayashi *et al.*: Research Report of LNS, Tohoku University **37** (2004) 17.

(LNS Experiment : #2564)

Energy Calibration of STB-Tagger II by Using e^+e^- Pair Production

K. Suzuki, R. Hashimoto, T. Ishida, T. Ishikawa, J. Kasagi, S. Kuwasaki, K. Mochizuki, K. Nawa, Y. Okada, Y. Onodera, H. Shimizu, and H. Yamazaki

Laboratory of Nuclear Science, Tohoku University, Sendai, 982-0826

The energy calibration of a bremsstrahlung tagging system STB-Tagger II was carried out by using a dipole magnet $\mathcal{R}$TAGX. The tagged photon energy was determined by a momentum analysis of e^+e^- pairs converted from bremsstrahlung photons at two energies of STB circulating electrons. The relative relation was obtained between the tagged photon energy for 920 MeV circulating electrons and that for 1200 MeV electrons. In this report, We present the method and the result of the energy calibration.

§1. Introduction

A tagged photon beamline has been constructed in the GeV-γ experimental hall at Laboratory of Nuclear Science (LNS), Tohoku University [1]. We insert a radiator made of a carbon fiber, 11 μm in diameter, into circulating electrons in the Stretcher-Booster (STB) ring to generate a high energy photon beam. The electrons strike the radiator just upstream from the bending magnet BM5 of the STB ring, and produce bremsstrahlung photons which are used as a beam. Recoiled electrons are analyzed by the BM5 and detected with a tagging system called STB Tagger II, which consists of 116 telescopes of two-layer scintillating fibers [2]. The energy E_γ of a produced photon is determined by the energy of the recoiled electron E_e and that of the circulating electron E_0 as

$$E_\gamma = E_0 - E_e$$

because the energy transferred to the nucleus is negligibly small. Thus E_e has to be measured precisely to provide a definite E_γ. However, there are some elements having slightly unknown factors in the STB Tagger II. The map of the magnetic flux in BM5 is not determined completely. The position and direction of the recoiled electron emitting a bremsstrahlung photon are not known precisely at the radiator. And the exact position of STB Tagger II is not well known. Therefore the energy calibration is required for STB Tagger II. To determine E_e, E_γ has to be given conversely, which has so far been made with two methods.

1. Missing mass M_X analysis for the $\gamma + p \rightarrow \pi^0 + X$ process [3], and
2. Direct Measurement of E_γ with a lead glass Cherenkov counter [4].

In the former method, however, there is an uncertainty in the vertex point of the π^0 decay, and the energy and position resolutions for incident photons are not good enough for this purpose. In the latter case, the energy response of the lead glass Cherenkov counter is not precisely investigated. These two methods did not work very well.

The tagged photon energy E_γ can be obtained by measuring momenta of the e^+e^- pair converted from the incident photon. E_γ is given as a sum of the e^+ and e^- energies E_{e^+} and E_{e^-}, namely

$$E_\gamma = E_{e^+} + E_{e^-}. \tag{1}$$

We have performed meson photoproduction experiments with an electro-magnetic calorimeter SCISSORS II to study nucleon resonances, using a tagged photon beam. Two circulating-electron energies of 920 and 1200 MeV have been selected to cover the incident photon energy from 600 to 1150 MeV. We can make a consistency check for STB Tagger II by comparing the overlap energy region measured under these different conditions of the electron energy. In this measurement, therefore, a dipole magnet $\mathcal{R}$TAGX [5] is operated at a fixed current to analyze the momentum of the e^+ and e^-, regardless of the electron energy.

§2. Experiment

We used the $\mathcal{R}$TAGX magnet for the momentum analysis of e^+e^- pairs. A 20 μm thick Au foil was placed in front of $\mathcal{R}$TAGX to produce e^+e^- pairs from the tagged photons. Electrons/positrons having different momenta were bent with different curvature by $\mathcal{R}$TAGX , and were detected with two scintillating fiber hodoscopes located behind $\mathcal{R}$TAGX. Each scintillating fiber measures 3×3 mm^2 in cross section, and 16 fibers are arranged in a hodoscope. One hodoscope was placed 1850 mm downstream from the center of $\mathcal{R}$TAGX and at -46.6° with respect to the beam axis. The other hodoscope was movable so as to detect various energy electrons. Figure 1 shows the experimental setup for this energy calibration.

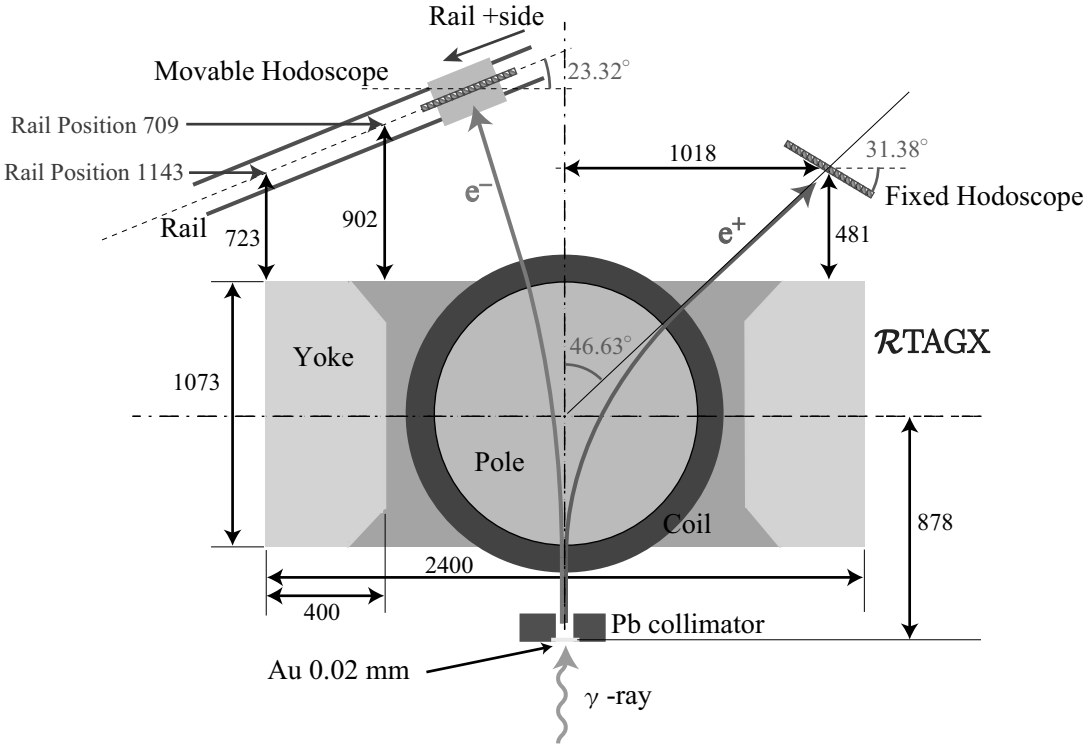

Fig.1. Experimental setup for the energy calibration of STB-Tagger II. The e^+e^- pairs are generated in the interaction of incident photons with a Au foil, and are detected by a fixed scintillating fiber hodoscope and a movable one.

A triple coincidence signal from STB-Tagger II and two scintillating fiber hodoscopes was used to form a trigger for the data acquisition:

$$(\text{trigger}) = (\text{tagger}) \otimes (\text{fixed hodoscope}) \otimes (\text{movable hodoscope}).$$

We measured the energy of each tagged photon defined with STB Tagger II using this trigger by detecting an e^+e^- pair generated from the tagged photon. The experiment was performed for two different electron energies of 920 and 1200 MeV.

§3. Data Analysis

A pair of e^+ and e^- were detected with the fixed and movable hodoscopes, respectively. Energies of e^+ and e^- were determined from the position of responding fibers in these hodoscopes. Here, the flight path of e^+/e^- with a given energy was calculated by utilizing the field map of $\mathcal{R}$TAGX, where the energy loss of e^+/e^- was taken into account in the Au foil and the air. The magnetic flux of $\mathcal{R}$TAGX is described elsewhere [6, 7]. Figure 2 shows the e^+/e^- energy as a function of the bending angle determined by a responding fiber.

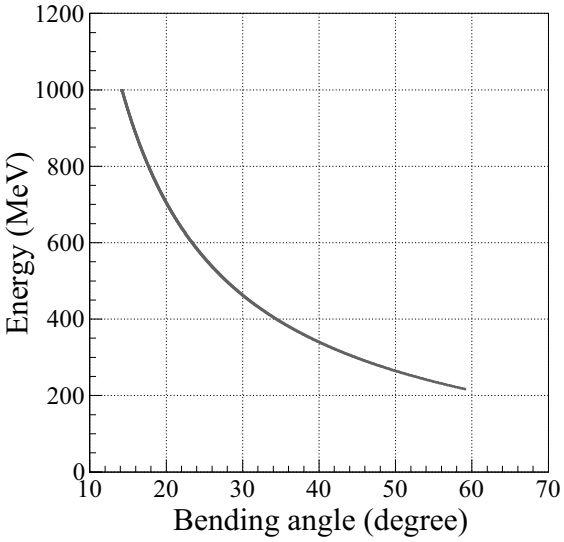

Fig.2. The e^+/e^- energy as a function of the bending angle.

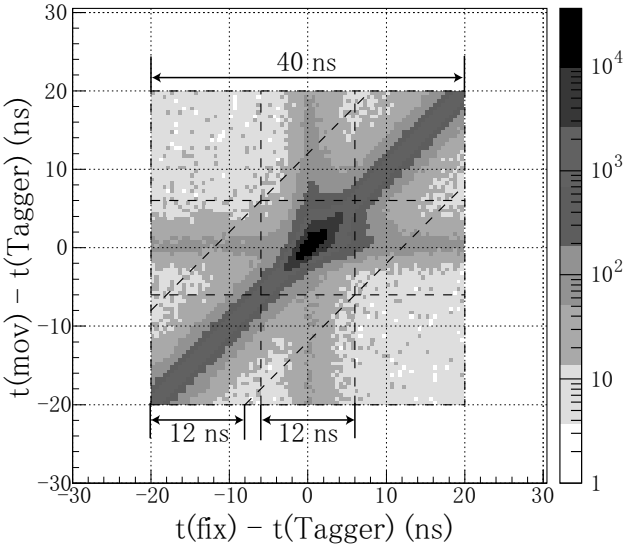

Fig.3. Timing Correlation between the movable and the fixed hodoscope.

Since the intensity of the bremsstrahlung photons was more than 10 MHz, there was a large fraction of accidental coincidence events. To estimate the number of true coincidence events, we made a two-dimensional plot of the timing signals from the movable and fixed hodoscopes. Figure 3 shows the timing correlation between the movable and fixed hodoscopes. The total area of the two-dimensional plot is divided into 16 regions by broken lines, the center region is the prompt area, and the other regions correspond to background events. The background events in the prompt area were subtracted with the method of two-dimensional side band subtraction. This method is described elsewhere [8, 11].

The energy of a tagged photon can be obtained with a sum of the e^+ and e^- energies as expressed in Eq. (1). Figure 4 shows e^+e^- energy sum distributions corresponding to tagger channel, 1, 70 and

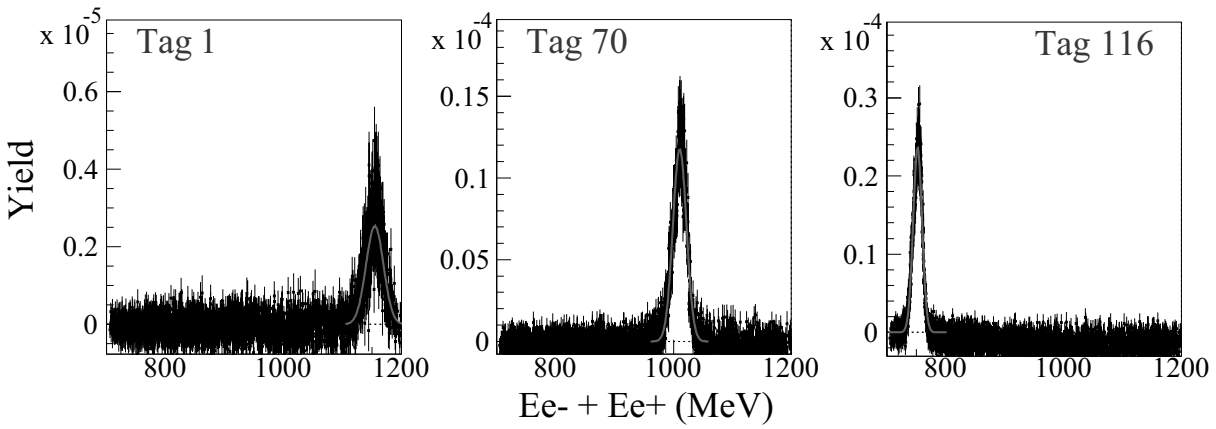

Fig.4. Energy sum distributions of e^+ and e^- converted from the tagged photons corresponding to tagger channel, 1, 70 and 116. Each curve is a Gaussian function fitted to the data.

116 after the background subtraction of accidental coincidence events. The centroid of the e^+e^- energy sum is determined by fitting a Gaussian function to the data.

§4. Tagged Photon Energy

The energy of photons tagged with STB Tagger II was calibrated by measuring the energies of e^+e^- pairs. STB-Tagger II covers the tagged photon energy range from 579 to 890 MeV for 920 MeV circulating electrons, and 752 to 1155 MeV for 1200 MeV electrons. Since the $\mathcal{R}$TAGX coils carried a fixed current, the tagged photon energy for 920 MeV electrons was determined relatively to that for 1200 MeV electrons. In Fig. 5, the measured photon energies are plotted as a function of the telescope number in STB Tagger II.

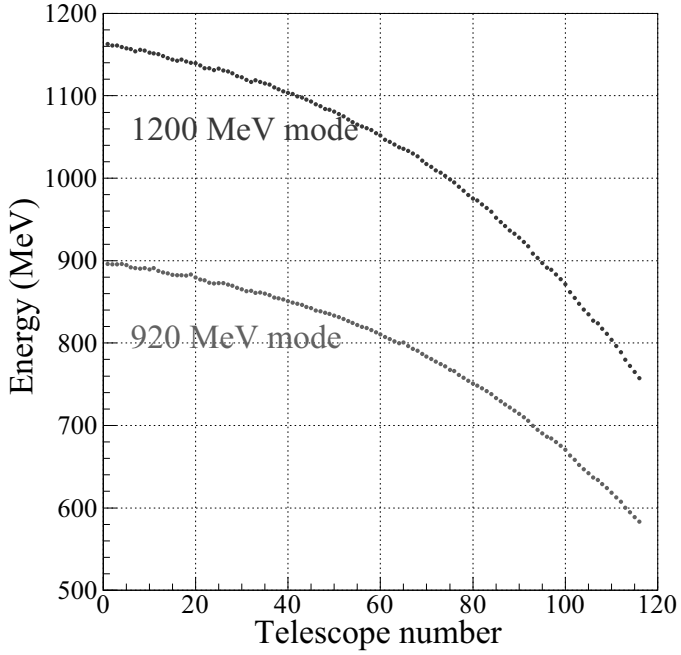

Fig.5. Relation between the photon energy and the telescope number in STB Tagger II at two circulating-electron energies of 920 and 1200 MeV.

We made another calibration by measuring the threshold energy of the $\gamma + p \rightarrow \eta + p$ reaction. This calibration identified the tagging telescope corresponding to the incident photon having the η production threshold energy. The threshold photon energy in the $\gamma + p \rightarrow \eta + p$ reaction can be calculated precisely, that is $E_\gamma = 707.25$ MeV. We compared the η threshold energy with the tagged photon energy corresponding to the η threshold point by the momentum analysis for e^+e^- pairs. It turned out that the tagged photon energy determined by the momentum analysis was 0.63% larger than the threshold energy [9]. This difference was mainly caused by an overall normalization uncertainty in the magnetic field of $\mathcal{R}$TAGX. Thus the normalization uncertainty was resolved [10]. The geometrical errors arise from a position measurement uncertainty of the fixed and movable hodoscopes, a setup uncertainty of the movable hodoscope location, and a position uncertainty of the incident photon beam [11]. The total uncertainty of the tagged photon energy is 0.3%.

References

[1] H. Shimizu *et al.*: Research Report of Laboratory of Nuclear Science, **37** (2004) 13.

[2] T. Nakabayashi *et al.*: Research Report of Laboratory of Nuclear Science, **37** (2004) 17.

[3] S. Suzuki: Master's thesis, Department of Physics, Tohoku University (2005).

[4] T. Ishikawa: Internal GeV-γ analysis note No.**15** (2006).

[5] T. Ishikawa *et al.*: Research Report of Laboratory of Nuclear Science, **39** (2004) 39.

[6] T. Ishikawa: Internal GeV-γ analysis note No.**20** (2006).

[7] T. Ishikawa: Internal GeV-γ analysis note No.**34** (2006).

[8] T. Nakabayashi: Internal GeV-γ analysis note No.**18** (2006).

[9] T. Ishikawa: Internal GeV-γ analysis note No.**57** (2007).

[10] K. Suzuki: Internal GeV-γ analysis note No.**59** (2007).

[11] K. Suzuki: Internal GeV-γ analysis note No.**35** (2007).

(LNS Experiment : #2536, #2582)

Performance of a Test Calorimeter of Lead Scintillating Fiber Modules

K. Mochizuki, T. Ishikawa, R. Hashimoto, T. Ishida, S. Kuwasaki, K. Nawa, Y. Okada, Y. Onodera, H. Shimizu, K. Suzuki, and H. Yamazaki

Laboratory of Nuclear Science, Tohoku University, Sendai, 982-0826

A new electro-magnetic (EM) calorimeter complex FOREST comprises three independent calorimeters, covering a solid angle of about 4π sr in total. The Backward Gamma detector brought from SPring-8/LEPS is employed to cover the central part of FOREST. Backward Gamma consists of lead scintillating fiber (Lead/SciFi) detector modules. The performance of a test calorimeter made up with 9 Lead/SciFi detector modules of Backward Gamma has been studied by using a positron beam with energies up to 800 MeV.

§1. Experimental Setup

The performance study of a test calorimeter was made at the electron/positron beamline dedicated to testing detectors at LNS. The test calorimeter is made up with Lead/SciFi detector modules stacked in a 3×3 array, which is a small portion corresponding to a polar angle from 60° to 90° of the Backward Gamma detector. Momentum-analyzed positrons were used as an incident beam with the energy ranging from 200 to 800 MeV . A beam profile monitor (BPM) was used to specify the position of the incident positrons. BPM consists of two layers of scintillating fiber (SciFi) hodoscopes. Each hodoscope is composed of 16 SciFi modules with a cross section of 3×3 mm^2. The upstream and downstream layers determine the x and y positions of the incident positron, respectively. Figure 1 shows the experimental setup for the performance study of the calorimeter.

The trigger condition for the data acquisition system is described as

$$[x \text{ fiber OR}] \otimes [y \text{ fiber OR}], \tag{1}$$

where $\otimes$ means coincidence of signals. The maximum trigger rate was 2 kHz and a fraction of accidental coincidence events was negligibly small. The energy calibration for the Lead/SciFi detector modules was made by using 300, 460, 590, and 800 MeV positrons injected on to the central region (6×6 mm^2) of each module one by one. The detector module has the shape of a truncated pyramid. Therefore the position and the tilted angle of the calorimeter were set so that the beam axis was perpendicular to the front face of the module of interest. Then the gain of each detector module was adjusted.

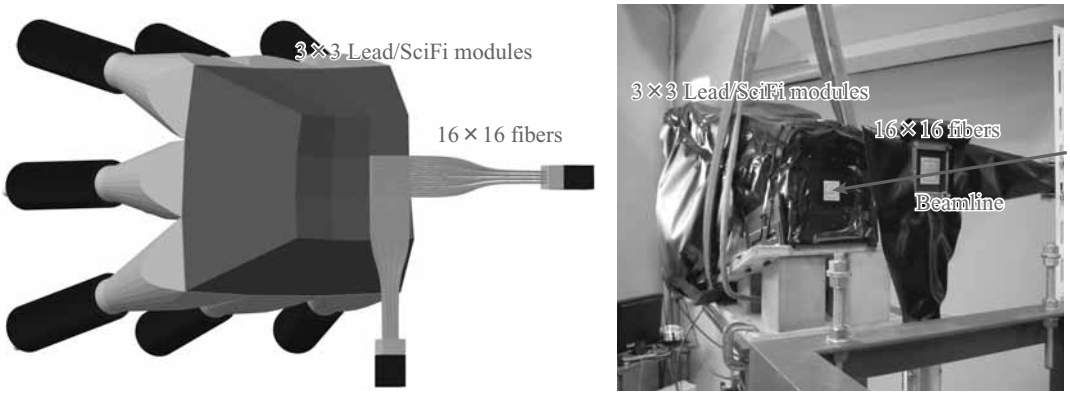

Fig.1. Experimental setup for the performance study of a test calorimeter comprised of 9 Lead/SciFi detector modules. The 16 × 16 scintillating fiber hodoscopes are placed in front of the calorimeter to determine the position of incident positions.

§2. Energy Response

The deposited energy in the calorimeter is obtained by summing up the measured energies with 9 detector modules as

$$E = \sum_{j=1}^{9} E_j. \tag{2}$$

The positrons injected on to the central region (6×6 mm^2) were selected in the energy measurement to suppress the energy leakage out of the detector modules in the lateral direction. The linearity of the energy response was checked with the ratio of the reconstructed energy to the incident positron energy. Figure 2a) shows the ratio as a function of the incident energy. The normalization of the reconstructed energy is arbitrary. A linear function $r_\mu(E_i)$ of the incident energy E_i was fitted to the measured ratio r_μ. The fitted result is expressed as

$$r_\mu(E_i) = (1.1307 \pm 0.0022) - (5.0769 \pm 0.3433) \times 10^{-5} E_i, \tag{3}$$

where E_i is in MeV. The non-linearity of the energy response was found to be less than 6% for the incident beam energies from 200 to 800 MeV.

The energy resolution σ_E/E can be evaluated with a Gaussian mean μ and a width σ of the reconstructed energy distribution as

$$\frac{\sigma_E}{E} = \left\{ \left(\frac{\sigma}{\mu}\right)^2 - \left(\frac{\sigma_b}{\mu_b}\right)^2 \right\}^{1/2}, \tag{4}$$

where the effect of beam energy spread σ_b/μ_b [3] is subtracted. Figure 2 b) shows the measured energy resolution as a function of the incident energy. The energy resolution σ_E/E may be expressed as

$$\frac{\sigma_E}{E} = \left\{ \left(\frac{a_2}{E}\right)^2 + \left(\frac{a_1}{\sqrt{E}}\right)^2 + a_0^2 \right\}^{1/2}. \tag{5}$$

The function (5) is fitted to the data to give the result,

$$\frac{\sigma_E}{E}(E_i) = \left\{ \left(\frac{1.93 \pm 0.11}{E_i}\right)^2 + \left(\frac{6.91 \pm 0.08}{\sqrt{E_i}}\right)^2 + (0.00 \pm 0.92)^2 \right\}^{1/2}, \tag{6}$$

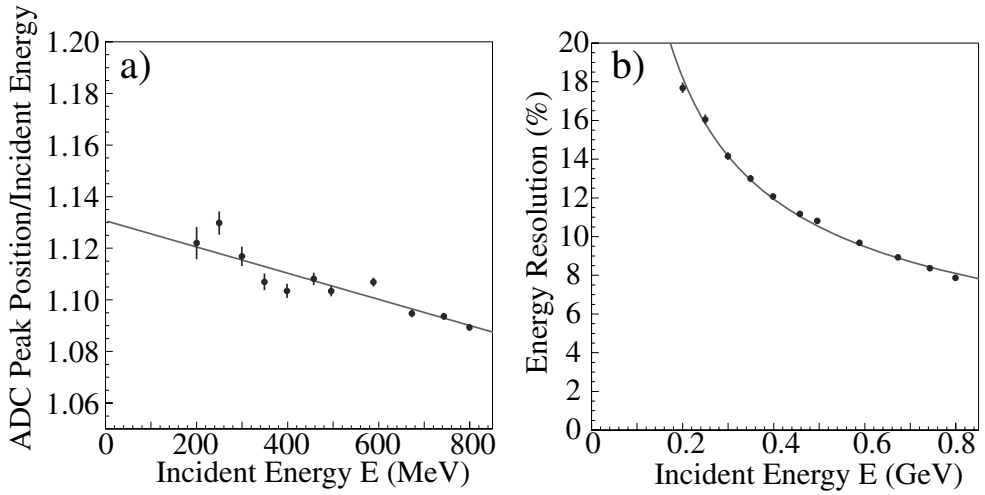

Fig.2. The energy response as a function of the incident positron energy. a) The ratio of the reconstructed energy to the incident energy. The normalization factor is arbitrary. The data are fitted with a linear parametrization $1.1307 - 5.0769 \times 10^{-5} E_i$. b) The measured energy resolution. The data are well expressed with the parametrization $\sqrt{(1.93/E_i)^2 + \left(6.91/\sqrt{E_i}\right)^2 + (0.00)^2}$.

where the parameters a_0, a_1, and a_2 are given in % and E_i in GeV, respectively. The energy resolution for 1 GeV positrons corresponds to 7.2%. The details of the analysis for the energy resolution are described elsewhere [4].

§3. Position Resolution

The incident position of positrons on the calorimeter was reconstructed by the energy weighted average of the position vectors $\vec{x}_i$ of 9 modules as

$$\vec{x}_r \propto \sum_{j=1}^{9} C_j E_j \vec{x}_j, \tag{7}$$

where the origin of the position vectors was the common center of a circumscribed sphere for front faces of the modules. The normalization was made in such a way that the length of the reconstructed position vector should be the radius of the sphere (300 mm). Since the energy deposit to the central module was much larger than that to the peripheral modules, the weight for the signal from the central module was set to be smaller by using an extra factor C_i:

$$C_j = \begin{cases} C_0 & \text{for the central module} \\ 1 & \text{for the peripheral modules} \end{cases} \tag{8}$$

The factor C_0 was determined for each incident energy so that the mean of the difference between the reconstructed position and the incident position determined by BPM would be 0. The determined values of C_0 are 0.01765 ± 0.00002, 0.02684 ± 0.00001, 0.02484 ± 0.00001, 0.02123 ± 0.00001, 0.02562 ± 0.00001, and 0.02473 ± 0.00001 for the incident energies of 300, 400, 500, 590, 670, and 800 MeV, respectively. The difference distribution has a Gaussian shape whose mean is 0 by using the determined C_0. The x (y) position resolution is estimated with the width σ_x (σ_y) which is obtained by fitting a Gaussian function

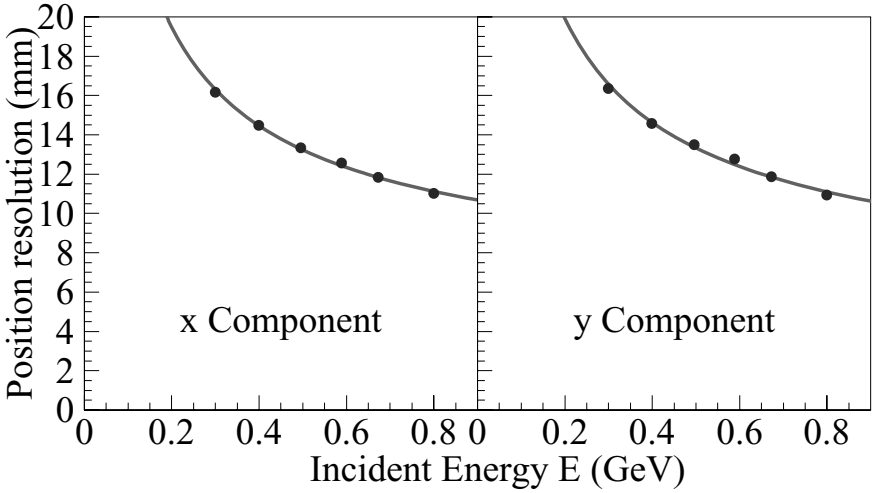

Fig.3. The position resolution as a function of the incident energy. The left and right panels show x and y components, respectively. The data are fitted with the form $\sqrt{(a_2/E_i)^2 + (a_1/\sqrt{E_i})^2 + (a_0)^2}$.

to the difference distribution in x (y) direction. Figure 3 shows the position resolution as a function of the incident energy. The position resolution σ_x and σ_y may also be represented with a similar function to Eq. (5). The fitted result are

$$\begin{cases} \sigma_x(E_i) = \left\{ \left(\dfrac{0.00 \pm 0.00}{E_i} \right)^2 + \left(\dfrac{8.27 \pm 0.03}{\sqrt{E_i}} \right)^2 + (6.18 \pm 0.07)^2 \right\}^{1/2} \text{ and} \\ \sigma_y(E_i) = \left\{ \left(\dfrac{0.00 \pm 0.00}{E_i} \right)^2 + \left(\dfrac{8.53 \pm 0.03}{\sqrt{E_i}} \right)^2 + (5.68 \pm 0.07)^2 \right\}^{1/2}, \end{cases} \tag{9}$$

where the position resolution σ_x (σ_y) and E_i are given in mm and GeV, respectively. The x and y position resolutions for 1 GeV positrons correspond to 10.3 mm and 10.2 mm, respectively. The details of the analysis for the position resolution are described elsewhere [5].

Acknowledgment

We appreciate Dr. T. Matsumura for fruitful discussions on the energy and position resolutions for the Lead/SciFi modules.

References

[1] T. Ishikawa, LNS Experiment #2536 (2005).

[2] T. Ishikawa *et al.*, Research Report of LNS, Tohoku University **39** (2006) 35.

[3] T. Ishikawa, Internal GeV-γ analysis note No.**43** (2007).

[4] K. Mochizuki, Internal GeV-γ analysis note No.**44** (2007).

[5] K. Mochizuki, Internal GeV-γ analysis note No.**46** (2007).

(LNS Experiment : #2536, #2582)

LEPS Backward Gamma Detector Reassembled

T. Ishikawa, K. Mochizuki, K. Suzuki, Y. Okada, R. Hashimoto, J. Kasagi, S. Kuwasaki, K. Nawa, Y. Onodera, M. Sato, H. Shimizu, and H. Yamazaki

Laboratory of Nuclear Science, Tohoku University, Sendai, 982-0826

A new electro-magnetic (EM) calorimeter complex FOREST covering a solid angle of about 4π sr is under construction. It consists of three calorimeters: the EPS forward one made up of pure CsI crystals, the middle one of lead scintillating fiber (Lead/SciFi) modules, and the backward one of lead glass Čerenkov counters. We have reassembled the middle calorimeter, comprised of 252 Lead/SciFi modules, which used to be the LEPS Backward Gamma detector system utilized in a LEPS experiment at SPring-8. A performance test for the gamma detector system has been made with a photon beam in the GeV γ experimental hall. The π^0 peak is clearly observed in the $\gamma\gamma$ invariant mass distribution.

§1. Electro-Magnetic Calorimeter Complex FOREST

Nucleon resonances were experimentally studied via π^0 and η photo-production by using an electromagnetic (EM) calorimeter SCISSORS II in the GeV-γ experimental hall at Laboratory of Nuclear Science (LNS), Tohoku University. The π^0 and η mesons are identified as a peak at specific places in the $\gamma\gamma$ invariant mass distribution. It was difficult, however, to detect all the γ's coming from π^0 or η decay since the solid angle of SCISSORS II was only 12.6% in total. In addition to that the process of multi-π production is dominant in the GeV energy region. There is a huge background made up with wrong combinations of γ's, which do not form a peak of π^0 nor η in the $\gamma\gamma$ invariant mass distribution. To suppress the background due to the wrong combinations, a large solid angle calorimeter is required so that a fraction of undetected γ's decreases.

A new EM calorimeter complex called Four-pi Omnidirectional Response Extended Spectrometer Trio (FOREST) with a solid angle of about 4π sr has been planed [1]. It consists of three calorimeters. The most forward region is covered with pure CsI crystals 'SCISSORS III' [2]. The detector system called 'Backward Gamma' is placed at the central region. And a set of lead glass Čerenkov counters covers the backward region. Figure 1 shows a schematic view of FOREST and a side view of Backward Gamma. The Backward Gamma detector system covers 30°–100° in the polar angle and 0°–360° in the azimuthal angle, consisting of 252 Lead/SciFi modules. Each module has a 10° coverage both in the polar and azimuthal angles. Backward Gamma was originally used at the Laser Electron Photon beam facility at SPring-8 (LEPS).

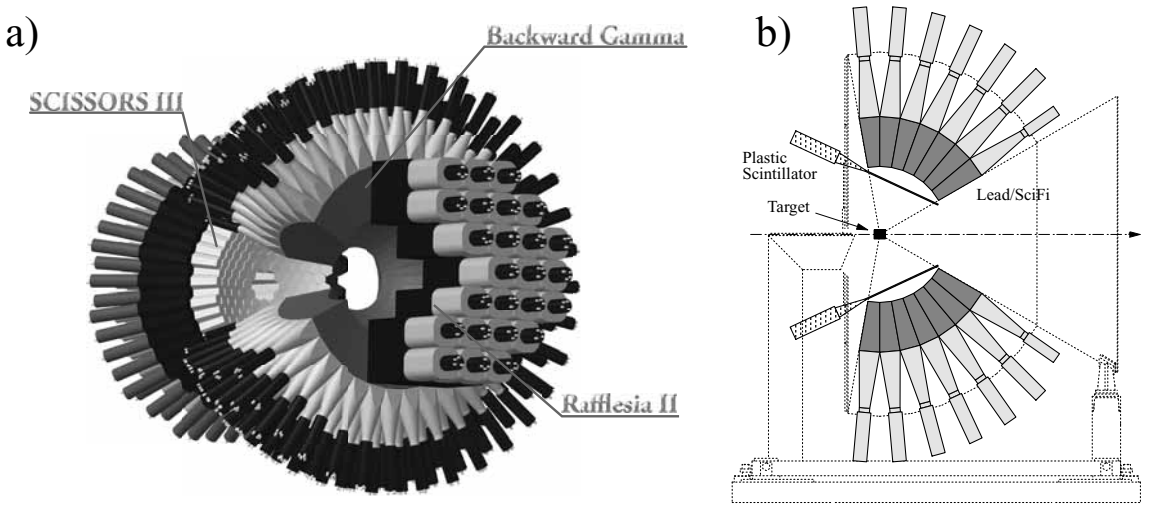

Fig.1. a) Slant view of the new EM calorimeter complex FOREST. b) Side view of the LEPS Backward Gamma detector. Backward Gamma consists of 252 Lead/SciFi modules. Each module covers 10° both in the polar and azimuthal angles.

§2. Rebuilding of LEPS Backward Gamma Detector

The LEPS Backward Gamma system was reassembled from 9th to 23rd Nov. in 2006. The frame of Backward Gamma was rotated first of all so that the plane corresponding to the polar angle of 90°

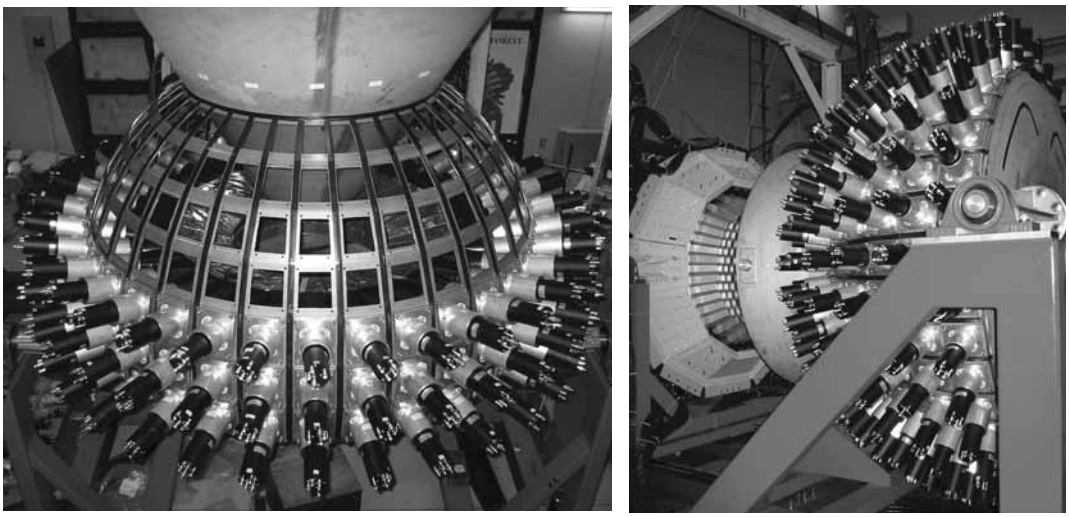

Fig.2. LEPS Backward Gamma. The left panel shows a photo of the LEPS Backward Gamma when the 90°–100°, 80°–90°, and 70°–80° Lead/SciFi modules were stacked. The right panel shows a photo of the constructed Backward Gamma together with SCISSORS III.

became horizontal. The largest Lead/SciFi modules covering a polar angle of 90°–100° were installed into the frame at first. Then 80°–90° modules were stacked on the 90°–100° ones. The 70°–80° and 60°–70° modules were installed in the same way. The left panel of Fig. 2 shows the middle stage of stacking procedure. The 50°–60°, 40°–50°, and 30°–40° modules of the same azimuthal angle were stacked at once so that the modules could not drop inside the frame during installation. The frame was rotated

back by 90°, after the installation of all Lead/SciFi modules was completed. Then the symmetry axis of Backward Gamma was aligned to the axis of the GeV-γ beamline.

§3. Beam Test for Backward Gamma Detector

A beam test of Backward Gamma was performed from 5th to 7th June in 2007. A data acquisition system for Backward Gamma was developed independently of that for the SCISSORS III. The energy deposited in each module was digitized with a LeCroy 4300B Fast Encoding and Readout ADC (FERA) in a CAMAC system. The data were collected and stored with a universal I/O (UIO) module [3] in a VME system through a LeCroy 4301 FERA driver in the CAMAC system. The timing signals were measured with CAEN V1190A TDC modules in the VME system. All the digitized data were finally accumulated in a personal computer (PC) through the VME-bus. The trigger signals are made under the condition

$$[\text{TotalSigmaTagger}] \otimes [N_{\text{BG}} \geq 2], \tag{1}$$

where TotalSigmaTagger stands for an OR signal of STB-Tagger II, and $N_{\text{BG}} \geq 2$ denotes the signal which is generated when more than two modules are responded.

The energy calibration was made in such a way that the position of the peak corresponding to π^0 events in the $\gamma\gamma$ invariant mass distribution should be at the π^0 mass. Figure 3b) shows the $\gamma\gamma$ invariant mass distribution measured with Backward Gamma. The π^0 peak is clearly observed.

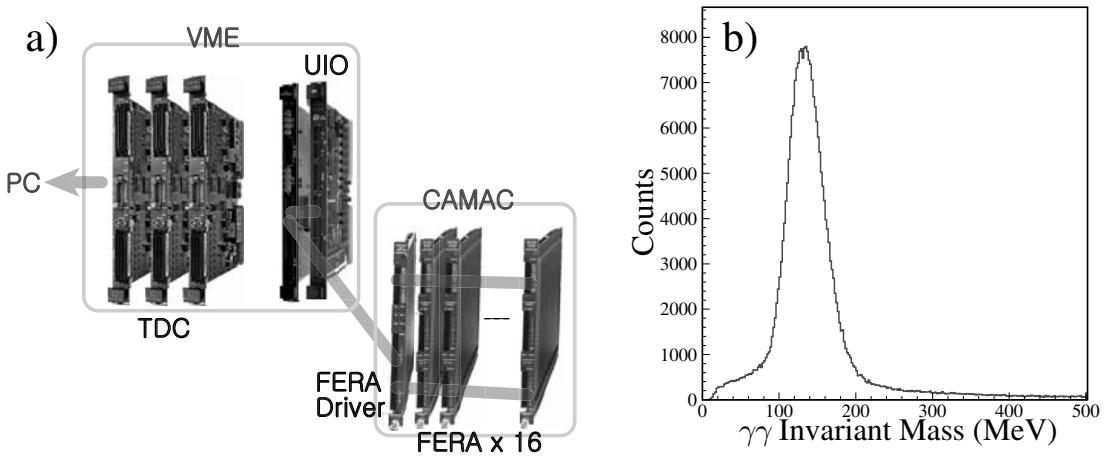

Fig.3. a) Dataflow of the data acquisition system for Backward Gamma. The digitized data of energies in FERA modules in a CAMAC system are collected in a UIO module through FERA driver. Those of timing signals are obtained with TDC modules in a VME system. b) The $\gamma\gamma$ invariant mass distribution measured with Backward Gamma. The π^0 peak is clearly observed.

Acknowledgment

We appreciate Dr. T. Yorita and Dr. T. Matsumura for many suggestions and advices in the re-assembling process of Backward Gamma.

References

[1] T. Ishikawa: LNS Experiment #2536 (2005).

[2] T. Ishikawa *et al.*: Research Report of LNS, Tohoku University **39** (2006) 35.

[3] Y. Sugaya and M. Nomachi: Nucl. Instrum. Methods Phys. Res., Sect. **A437** (1999) 68.

(LNS Experiment : #2582)

Current Status of the Electro-Magnetic Calorimeter SCISSORS III

T. Ishikawa, R. Hashimoto, J. Kasagi, S. Kuwasaki, K. Motiduki, K. Nawa, Y. Okada, Y. Onodera, M. Sato, H. Shimizu, K. Suzuki, and H. Yamazaki

Laboratory of Nuclear Science, Tohoku University, Sendai, 982-0826

A new electro-magnetic calorimeter complex FOREST with a solid angle of about 4π in total is under construction. A forward calorimeter SCISSORS III, a part of FOREST, was constructed last year. We have installed plastic scintillator hodoscopes in front of SCISSORS III. A beam test has been performed for the forward detector assembly. The π^0 peak is clearly observed in the $\gamma\gamma$ invariant mass distribution.

§1. Plastic Scintillator Hodoscopes in Front of SCISSORS III

Nucleon resonances are experimentally studied via π^0 and η photo-production by using an electromagnetic (EM) calorimeter in the GeV-γ experimental hall [1] at Laboratory of Nuclear Science (LNS), Tohoku University. These neutral mesons are identified in $\gamma\gamma$ invariant mass distributions. A new EM calorimeter complex called FOREST (Four-pi Omnidirectional Response Extended Spectrometer Trio) with a solid angle of about 4π in total is under construction [2] to reduce a fraction of undetected γ's. It consists of three calorimeters. A forward one made up of pure CsI crystals 'SCISSORS III' was constructed last year [3]. Since an EM calorimeter itself cannot distinguish whether an incident particle is neutral or charged, a thin plastic scintillator hodoscope is usually placed in front of it. We have designed and constructed a set of plastic scintillator hodoscopes named Spiral-shaped Particle Identification Detector for Elementary Reactions (SPIDER), which is capable of determining the incident position of charged particles precisely.

SPIDER consists of 3 layers, each of which is made up of 24 identical plastic scintillators. The side curve of each plastic scintillator has a shape of spiral as depicted in Fig. 1. The spiral curve may be represented as

$$r = \exp\{b(\theta + \theta_0)\}, \tag{1}$$

in the polar coordinate system, where r is a radius measured in mm, and b is a curvature parameter being chosen to be 1.1. The inside and outside radii r range from 57 to $425(1 - 0.15\sin 15^\circ)$ mm and to $425(1 + 0.35\sin 15^\circ)$ mm, respectively. The phase difference in θ between adjacent scintillators is 15°.

Two layers in SPIDER have different configurations in placing 24 spiral scintillators in a plane. One of them is a left-handed layer and the other is right-handed. A pair of these left-handed and right-handed layers can determine the position of charged particles going through SPIDER. The third layer is placed so as not to have inefficient area taking place at the boundary region of spiral in each scintillator.

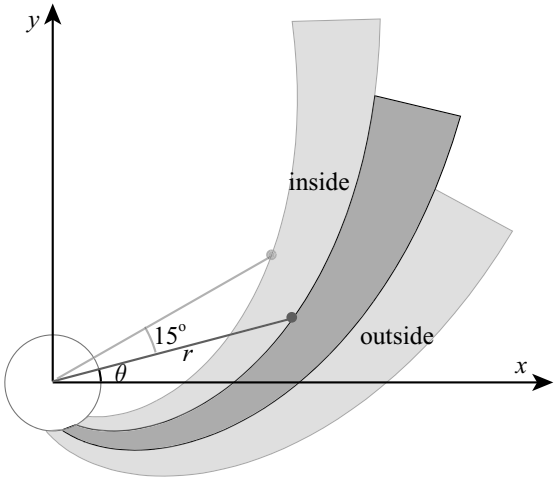

Fig.1. Spiral-shaped scintillators. The side curve of each plastic scintillator is represented as $\boldsymbol{r} = \exp\{\boldsymbol{b}(\boldsymbol{\theta} + \boldsymbol{\theta}_0)\}$ in the polar coordinate system. The phase difference between adjacent scintillators is 15°.

Figure 2 shows the schematic view and photo of SPIDER. The spiral-shaped scintillator is connected to a metal packaged photo-multiplier tube Hamamatsu R8900U through a twisted-type light guide.

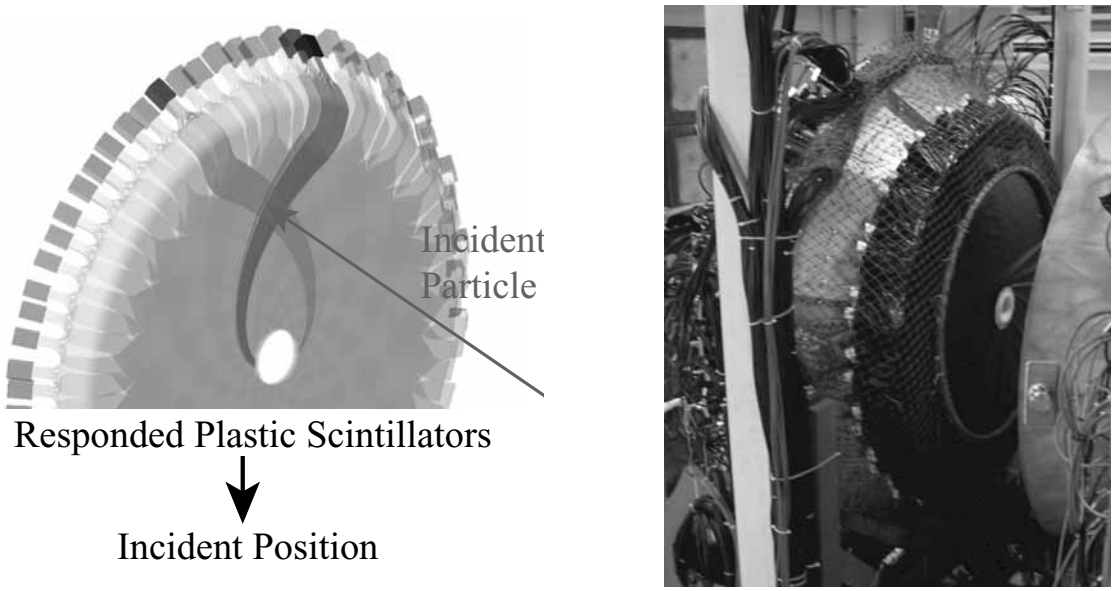

Fig.2. Schematic view and photo of SPIDER. The left panel illustrates how to reconstruct the incident position of charged particles. The right one shows the mounted SPIDER in front of SCISSORS III.

§2. Beam Test of SCISSORS III

A beam test of SCISSORS III with SPIDER was performed from 3rd to 5th Jul. in 2007. A data acquisition system for SCISSORS III was essentially the same as that for SCISSORS II. The energy and timing of each crystal were digitized by ADC and TDC modules in two TRISTAN/KEK Online (TKO) systems [4]. The digitized data were collected and stored with Super Memory Partner (SMP) modules

in a VME system through Super Control Header (SCH) modules in the TKO systems. All the digitized data were finally accumulated in a personal computer (PC) through the VME-bus. Figure 3a) shows a dataflow of the data acquisition system for SCISSORS III.

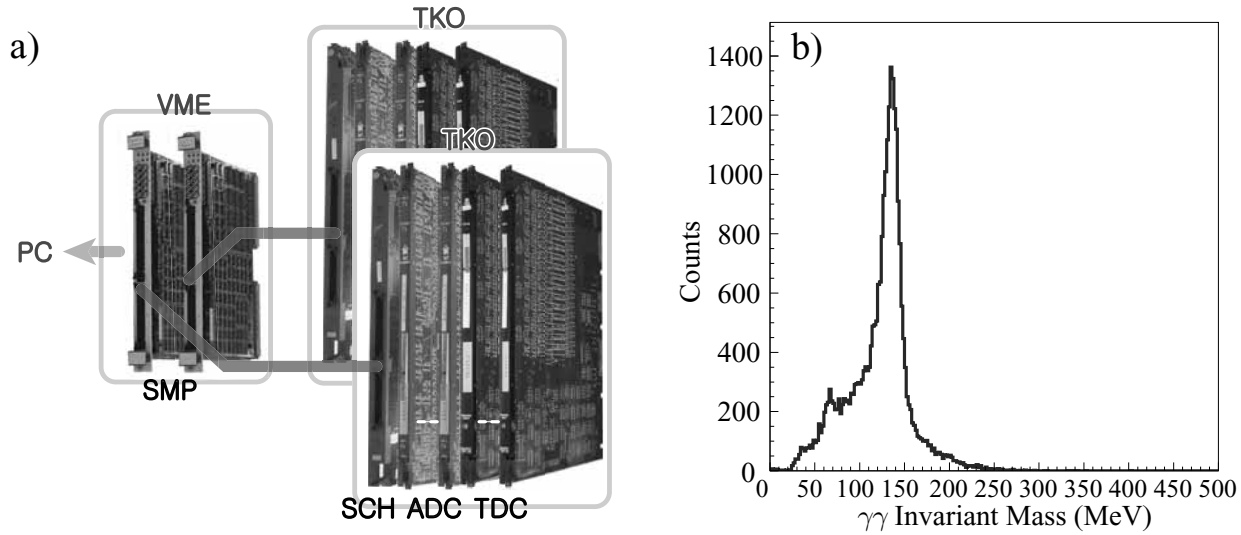

Fig.3. a) Dataflow of the data acquisition system for SCISSORS III. The digitized data of energies and timings are collected from ADC's and TDC's in a TKO system through SCH and SMP modules. b) The $\gamma\gamma$ invariant mass distribution measured with SCISSORS III. The π^0 peak is clearly observed.

The trigger condition was described as

$$\sum_i \left([\text{SigmaTagger } i] \otimes [N_{\text{S3}} \geq 2] \right), \tag{2}$$

where $\otimes$ means coincidence of signals. Channels of STB-Tagger II [5] were divided into 16 groups so that the counting rate of each group should be the same, and an OR signal of each group is denoted by SigmaTagger i ($i = 1 \ldots 16$). Crystals of SCISSORS III were divided into 10 groups; a signal of each group was generated when an analogue sum signal of the group exceeded the threshold. The $N_{\text{S3}} \geq 2$ stands for the signal in which more than two groups generate signals. A coincidence signal between SigmaTagger i and $N_{\text{S3}} \geq 2$ signals is required for taking data. Data can be taken with a higher intensity tagged photon beam in this condition compared with the condition:

$$\left(\sum_i [\text{SigmaTagger } i] \right) \otimes [N_{\text{S3}} \geq 2]. \tag{3}$$

A neutral cluster was selected as a γ particle, and the incident position is reconstructed by an energy weighted average of the position vectors of the modules which joins the cluster. The energy calibration is made so that the π^0 peaks in the $\gamma\gamma$ invariant mass distribution should be π^0 mass, where the events are selected by the condition that both the cluster energies are larger than 200 MeV. Figure 3b) shows the $\gamma\gamma$ invariant mass distribution measured with SCISSORS III. The π^0 peak is clearly observed.

References

[1] H. Shimizu *et al.*, Research Report of LNS, Tohoku University **37** (2004) 13.

[2] T. Ishikawa, LNS Experiment #2536 (2005).

[3] T. Ishikawa *et al.*, Research Report of LNS, Tohoku University **39** (2006) 35.

[4] KEK Data Acquisition Development Working Group, KEK Report 85-10 (1985).

[5] T. Nakabayashi *et al.*, Research Report of LNS, Tohoku University **37** (2004) 17.

Development of a Multi-Purpose Logic Module with the FPGA

K. Nanbu , T. Ishikawa , and H. Shimizu

Laboratory of Nuclear Science, Tohoku University, Sendai, 982-0826

We have developed a multi-purpose logic module (MPLM) with an FPGA. The internal circuit of this module can be modified easily with the FPGA. This kind of module enables trigger pulse processing for nuclear science. As a first step, the MPLM is used as an event tag generator in experiments with the FOREST detector system.

§1. Introduction

The structure and production mechanism of hadrons have been experimentally investigated via meson photo-production in Laboratory of Nuclear Science, Tohoku University. Nucleon resonances will be studied intensively with an electro-magnetic calorimeter complex FOREST in the GeV-γ experimental hall. Since the number of detectors in the FOREST is about 800, a set of logic modules for specified purposes is expensive. Therefore, a multi-purpose logic module with a field programmable gate array (FPGA) has been developed.

§2. Feature of FPGA

An FPGA is a semiconductor device which is programmable for any logic function by a designer. The FPGA is usually slower than an application-specific integrated circuit (ASIC). Since the ASIC cannot be modified after the design is completed, it is difficult to handle an ASIC to implement a specified design without bugs. On the other hand, the FPGA can be reconfigurable like software on a personal computer after it is manufactured. It is easy to shorten designing time to obtain the specified logic function by a trial-and-error method.

The FPGA contains programmable logic components called logic blocks, and programmable interconnects. Logic blocks can be programmed to operate simple or combinatorial functions of basic logic gates (AND, OR, XOR, flip-flops, and so on). The FPGA manufactured by Xilinx contains configurable logic blocks (CLB), input/output blocks (IOB), block random access memories (RAM), multipliers, and digital clock managers (DCM). The internal circuit of FPGA is constructed by connecting these elements.

The behavior of FPGA is usually defined with a hardware description language (HDL). Configuration data of logic blocks and interconnects which are fitted to the actual FPGA architecture are generated by a FPGA design software. The data are typically downloaded via a Joint Test Action Group (JTAG)

link cable.

§3. Multi-Purpose Logic Module

We have developed a logic module called Multi-Purpose Logic Module (MPLM) with an FPGA. This module is packaged in a single-width nuclear Instrumentation module (NIM) module. Figure 1 shows a photo of the MPLM. The FPGA used is a Xilinx SPARTAN3, and contains 4320 flip-flops (FF), 256 Kbit RAM, and 200,000 system gates.

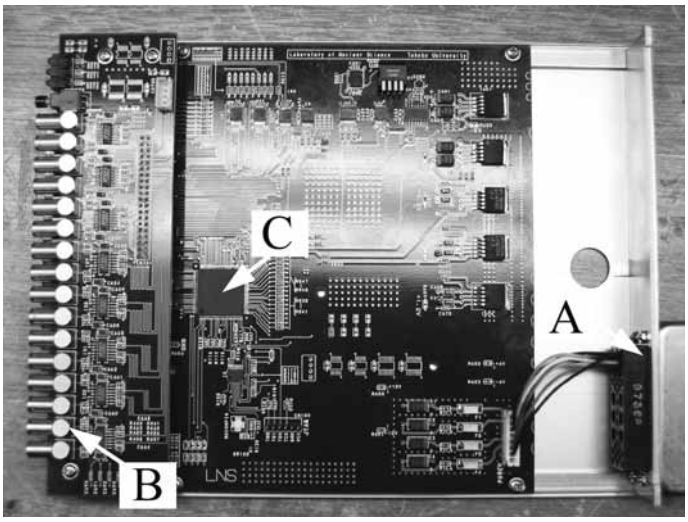

Fig.1. The MPLM (A: Bin power, B: LEMO Connector, C: FPGA).

This newly developed module accepts NIM standard signals, through 16 input and output channels. Since the FPGA does not accept the NIM signal, additional level converters between the NIM standard and the Low Voltage Transistor-Transistor Logic Level (LVTTL) signals are employed. The propagation delay from the input to the output is less than 10 ns, in which the conversion time from the NIM to LVTTL signals is dominant.

Figure 2 shows the block diagram of the MPLM. The MPLM contains 16 inputs with NIM to LVTTL converters, 16 outputs with LVTTL to NIM converters, a peripheral circuit for the configuration of the FPGA, a clock signal, and 3 status light emitting diodes (LED). The clock signal is generated by a crystal oscillator with a frequency of 33.33 MHz, and the frequency stability is better than 100 ppm. The FPGA receives a clock signal through a built–in global buffer (GBUF). The power source for many devices in the MPLM is provided through regulated power supplies as shown in Fig. 2. The MPLM supports the In-System Programming (ISP) through the JTAG interface, and a FPGA configuration system in a Platform Flash Memory (PROM). This module detects failures of the clock signal and those of power system. An RS-232C interface to a personal computer is optionally available. An operational amplifier (OPAMP) is operated with a higher frequency to shorten the leading time of the NIM standard signal ($\sim$3 nsec). The input impedance of the OPAMP is rather low for the FPGA. Nevertheless, the generated signal with the

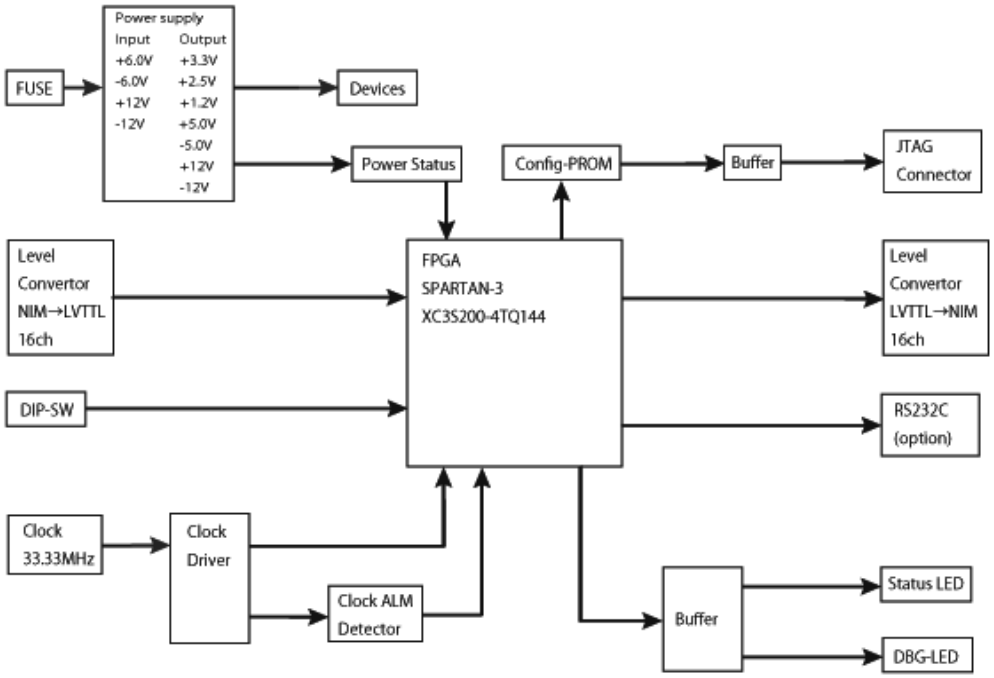

Fig.2. Block diagram of the MPLM.

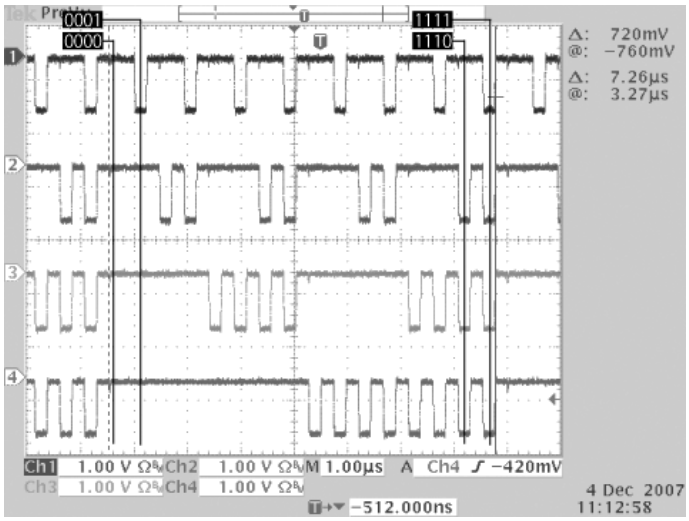

Fig.3. Timing diagram of the 4bit binary counter implemented in the MPLM. The 1st and 4th channels correspond to the lowest and most significant bits, respectively.

OPAMP meets the NIM standard although some reflection is observed in a pulse of the signal due to the impedance mismatch. Since this module is constructed on a 4 layer printed-circuit board (PCB), the impedance of the power system is reduced, which results in the noise level suppressed, in addition the high frequency operation allows the use of surface-mount components.

As a first step, this module is used as an event tag generator in experiments. A data taking system for FOREST is divided into several subsystems to collect digitized data with a short dead time. The

event tag is important to check event consistency whether digitized data collected by these subsystems belong to the same event or not. When the generator receives a trigger accept signal, a 4 bit associated event tag is generated. Figure 3 shows the operation of a 4 bit binary counter in the MPLM.

§4. Conclusion

A Multi-purpose Logic Module has been developed. This kind of module is necessary to handle digitized data efficiently under complicated trigger conditions.

(LNS Experiment : #2581)

Radiation Hardness Test of GaN Diode for Irradiation with High Energy Electron Beam

S. Narita[1], Y. Yamaguchi[1], Y. Chiba[1], H. Yuki[2], F. Hinode[2], and J. Kasagi[2]

[1]*Department of Electrical and Electronic Engineering, Iwate University, Morioka, 020-8551*
[2]*Laboratory of Nuclear Science, Tohoku University, Sendai, 982-0826*

The GaN is expected to be a new material for the particle detector with radiation hardness, as substitution of Si. We have developed the GaN Schottky diode which is a prototype of the ionizing detector. In this study we performed the test of radiation tolerance for the diode we fabricated, irradiating a high energy electron beam. As the result, we found that the performance of the diode was not changed significantly even after irradiating 10^{16}/cm^2 electrons.

§1. Introduction

In high-energy collider experiments, the beam luminosity has been increasing, and a semiconductor detector with radiation hardness is strongly desired in the current and future experiments. Several semiconductor materials have been investigated for developing new particle detectors as the substitution of Si [1, 2]. Among them, a wide-gap nitride semiconductor, especially gallium nitride (GaN), is one of the possible candidates. Recently, GaN devices have been widely used (e.g., light emitting device) and the technology to produce high quality substrate has been improved remarkably, so that development of the particle detector with GaN is now promising [3].

We have been developing the GaN based particle detector and successfully fabricated the GaN Schottky diode which has high quality in electrical and optical characteristics. Now it enables us to realize the GaN particle detector. In this study, we irradiated the diodes with high energy electrons and discussed the radiation hardness of GaN material.

§2. Experiment

2.1 GaN diode sample

The Schottky barrier diodes used in this study were fabricated with heterostructure substrate produced by Powdec K.K. growing an epitaxial GaN layer on n-type SiC substrate. Most of the current GaN devices are based on GaN on Sapphire substrate. For the Schottky diode device using GaN/Sapphire substrate, both Schottky and Ohmic contacts have to be made on the same surface because Sapphire is insulator. However, the diode with such a structure is not preferred to use for the particle detector because the device design is complicated and its sensitive area is limited. On the other hand, the diode with GaN/SiC substrate can be designed more simply due to the electric conductivity of SiC. The Ohmic contact can be put on the SiC side. The diode structure is shown in Fig.1.

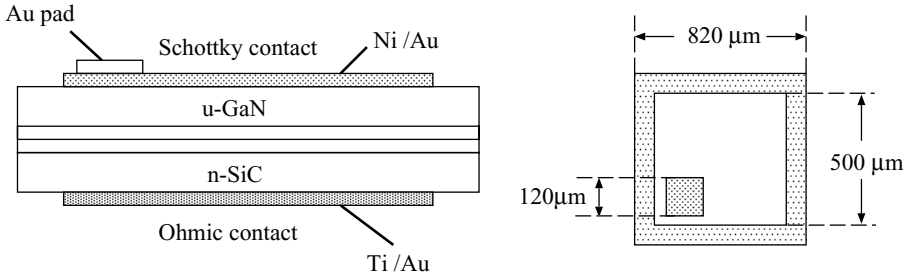

Fig.1. GaN diode structure.

The chip size of the diode was 0.5×0.5 mm^2, and the thickness of the GaN and SiC layers were $\sim$900 and $\sim$280 nm, respectively. The Ti/Au Ohmic contact was deposited on to the SiC and the Schottky Ni/Au electrode was put onto the GaN layer. For the irradiation test, the diode was placed onto the metal package. The current-voltage (I-V) characteristics of the diodes were measured by the ultra high resistance meter (ADVANTEST R8340). The leakage current was well suppressed ($\sim$10 nA/cm^2) and the breakdown voltage was typically above 20V. These performances were comparably good to the present GaN diode. We also investigated the photo-conductivity to the UV light, and it showed a good performance as the photo diode. Actually, the thickness of the sensitive layer was too thin to evaluate the performance for the charged particle (even for, e.g., α particles), for now.

The I-V characteristics were measured before and after irradiation in order to determine the effects of the incident electrons.

2.2 Electron beam irradiation

Beam irradiation was carried out at Laboratory of Nuclear Science, Tohoku University (LNS), using a 150 MeV pulsed electron beam. The beam current was measured by the SEM placed at the downstream of the target diodes. The conversion factor from the SEM current to the beam current was calibrated in advance of the experiment, which has about 30% uncertainties. The mean beam current value in this experiment was found to be 2.5 μA. We assumed that the beam condition was stable during the irradiation, then the current measurement was employed just once in prior to the irradiation. In this experiment, we prepared several diodes and irradiated them with electrons with various fluences. During the irradiation, the target diodes were not applied voltage, then the output currents from the diode were not monitored.

The beam profile was measured by the radio-activity of aluminum foil irradiated with the electron beam with the same conditions in the irradiation to the diodes. After irradiating the foil, the activity of the segmented area of the foil was measured by a Ge detector. The profiles along X and Y axes with the fitted Gaussian curves are shown in Fig.2. The electron fluences on the diode were obtained considering the mean current of the beam and these profiles. The fluence for each sample is shown in Table 2.2. The errors in the list were from the uncertainties of the SEM calibration data.

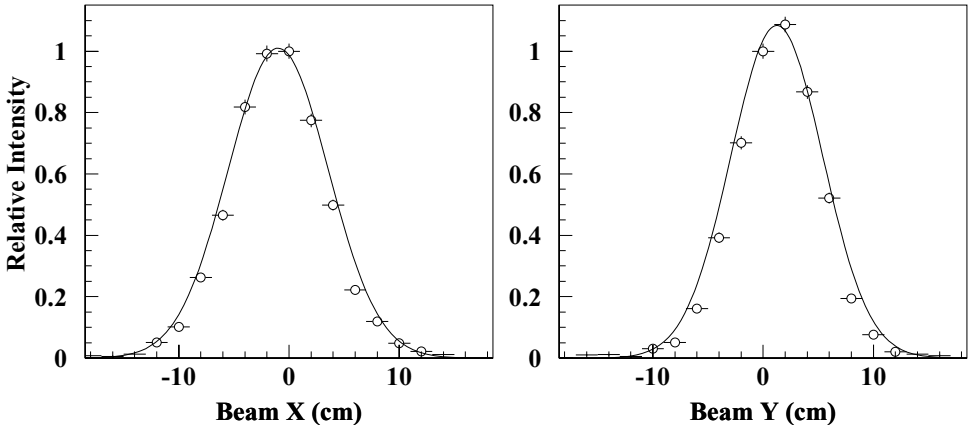

Fig.2. Beam profile fitted with the Gaussian. (left:X, right:Y). The fitted curves represent $f(x) = 1.01e^{\frac{(x+0.98)^2}{6.44^2}}$ for X-axis and $f(y) = 1.08e^{\frac{(y-1.24)^2}{5.90^2}}$ for Y-axis, respectively.

Table 1. Calculated electron fluences for each sample.

	Electron fluence $[/cm^2]$
Sample 1	$2.2 \pm 0.7 \times 10^{14}$
Sample 2	$2.2 \pm 0.7 \times 10^{15}$
Sample 3	$1.8 \pm 0.4 \times 10^{16}$
Sample 4	$3.4 \pm 1.0 \times 10^{16}$

§3. Results and Discussion

Figure 3 shows the I-V curves before and after irradiation for each fluence. No significant increase of leakage currents was seen even with the electron fluences above 10^{16}/cm^2. The break down voltage was not changed clearly. These results would prove the radiation hardness of the GaN.

The degradation of the semiconductor detector is strongly dependent on the energy loss of particles irradiated in both non-ionizing (atomic displacement) and ionizing (form of electron-hole pair) processes in the material. The non-ionizing energy loss of a 150 MeV electron is estimated to be 0.1 keV cm^2 g^{-1} [4], and this is smaller than that of other charged particles and a neutron. Besides the type of the particles, we should consider that the thickness of the diode used in this experiment was just $\sim 1\mu$m. The particle detectors used practically have much thicker structure, so that non-ionizing and ionizing effects are supposed to increase in such detectors. Therefore we still need to perform the irradiation test using heavy charged particles such as protons or α particles to discuss precisely the radiation hardness of the GaN material. Furthermore, we should repeat the test with changing the experimental conditions since the damage effects depend on various parameters (e.g., with/without applying the voltage, temperature, device structure, and so on).

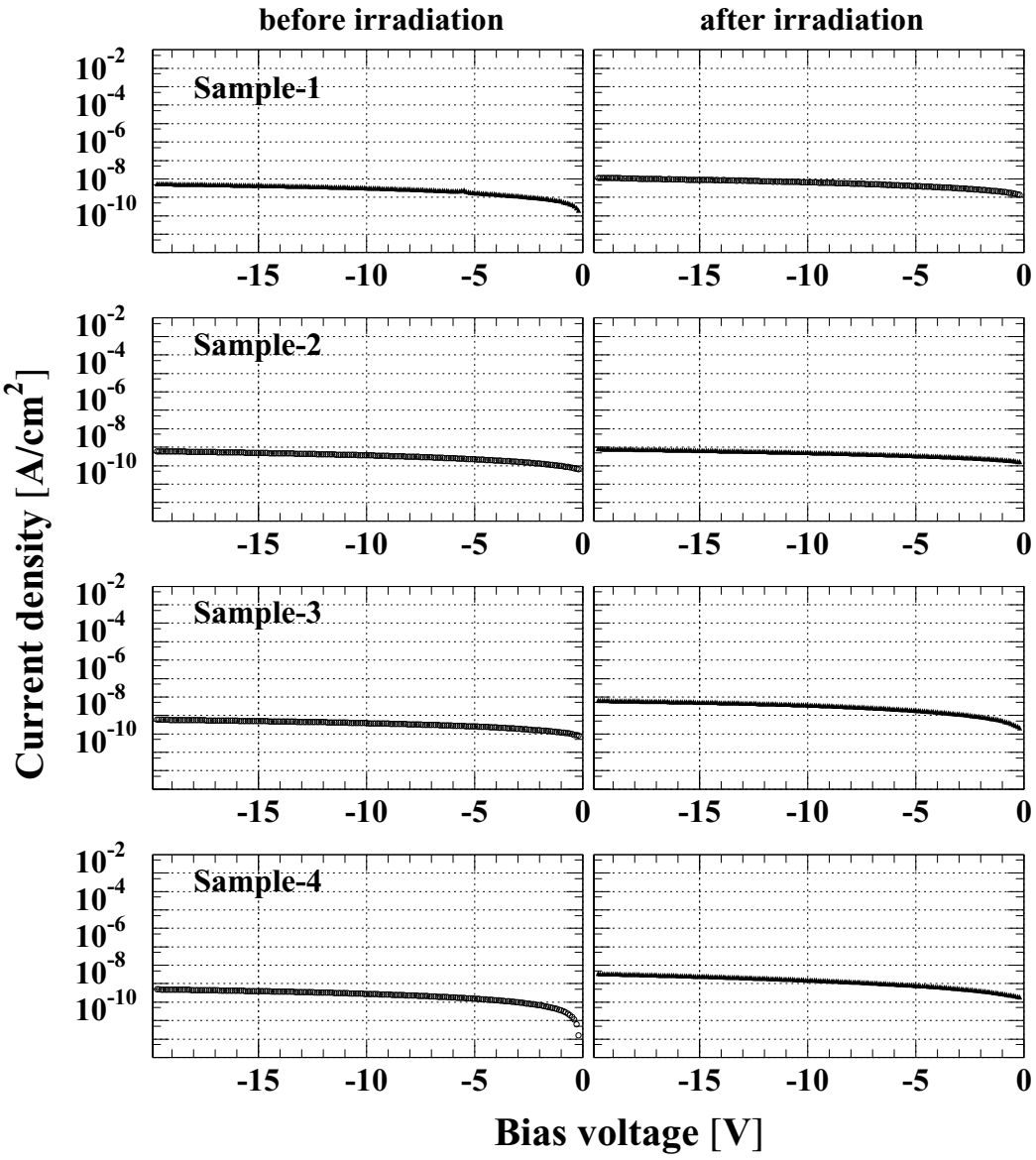

Fig.3. Current-Voltage characteristics for the sample before and after electron beam irradiation.

§4. Summary

We have evaluated the tolerance of the GaN material for the radiation damage irradiating with high energy electron beam. The performance was not significantly changed after irradiating 10^{16} /cm^2 electrons. The GaN might be a promising candidate for the material of future particle detectors. We should keep investigating the performance under various conditions and ensure the advantages.

Acknowledgment

We acknowledge technical and scientific staffs of the LNS. This work was supported by Grant-in-Aid for Young Scientists (B) by the Ministry of Education, Culture, Sports, Science and Technology (MEXT).

References

[1] M. Moll: Nucl. Instrum. Methods Phys. Res., Sect. A **511** (2003) 97.

[2] J. Grant *etal*.: Nucl. Instrum. Methods Phys. Res., Sect. A **546** (2005) 213.

[3] J. Vaitkus *etal*.:Nucl. Instrum. Methods Phys. Res., Sect. A **509** (2003) 60.

[4] A. Holmes-Siedle and L. Adams: "Handbook of Radiation Effects" (Oxford University Press, 2001).

(LNS Experiment : #2587)

J-PARC実験用ゲルマニウム検出器の波形読み出し法の開発

細見健二 [1], **鵜養美冬** [2], **大谷友和** [1], **小池武志** [1], **馬越** [1], **三森雅弘** [1], **三輪浩司** [1], **白鳥昂太郎** [1], **田村裕和** [1]

[1] 東北大学大学院理学研究科 (980-8578 仙台市青葉区荒巻字青葉)
[2] 東北大学サイクロトロン・ラジオアイソトープセンター (980-8578 仙台市青葉区荒巻字青葉)

Development of Waveform Readout System for Germanium Detectors at J-PARC

K. Hosomi[1], M. Ukai[2], T. Otani[1], T. Koike[1], Y. Ma[1], M. Mimori[1], K. Miwa[1], K. Shirotori[1], and H. Tamura[1]

[1]*Department of Physics, Tohoku University, Sendai, 980-8578*
[2]*Cyclotron and Radioisotope Center, Tohoku University, Sendai, 980-8578*

The waveform of signals from a germanium detector was measured by a Flash ADC under the high counting condition by a positron beam at LNS. Even if a baseline is shifted after preamp reset, the original energy was obtained by analyzing the waveform. The effectiveness of the wavefrom readout for J-PARC experiments was shown.

§1. はじめに

現在、我々のグループは J-PARC においてハイパー核ガンマ線分光実験 [1]を行うため、新型のゲルマニウム検出器アレイ「Hyperball-J」を建設中である。J-PARC で実験を行う際、旧 Hyperball 用の読み出し方法を用いた場合には、ビーム強度の増加にともなう不感時間の増加から 2 MHz 以上のビーム強度ではデータ収集が行えないと予想される。第 1 表に J-PARC で予想される実験条件を示した。旧 Hyperball 用の読み出し方法はプリアンプ、整形アンプ、パルス波高型 ADC という流れでゲルマニウム検出器に入ったエネルギー情報を波高情報に変換して読み出す方式になっており、不感時間を生じる要因は以下の２つである。１つ目はプリアンプのリセットである。運動量が GeV オーダーの中間子ビームを使って実験を行うため、散乱ビームなどによる高いエネルギー付与率に耐えられるよう、低増幅率のトランジスター・リセット型のプリアンプを使っている。しかし、プリアンプのリセット時には、その後の数 10 μ 秒間は整形アンプのベースラインが変動してしまい正しい波高を得ることができず不感時間を生じる。もう１つは波形同士のパイルアップである。この場合もリセット直後と同様に正しい波高情報を得ることができず不感時間となる。

この問題を解決するため、Hyperball-J ではフラッシュADC を用いた波形読み出し法に変更する予定である。これは、整形アンプ出力を波形情報のまま記録し、オフライン解析によりリセット直後のベースライン補正とパイルアップの分離を行おうというものである。本来ならプリアンプ出力を直接フラッシュADC

で読み出すべきなのだが、フラッシュADC の性能によりエネルギー分解能が制限*されてしまうため、現段階では整形アンプ出力を読み出すこととする。

第 1 表　ハイパー核ガンマ線分光実験の条件。

	K6 (KEK) 実測値	K1.8 (J-PARC) 予想値
ビーム強度	2 MHz (π^+)	〜10 MHz (K^-)
カウントレート	50 kHz	〜250 kHz
エネルギー付与率	〜0.5 TeV/s	〜2.5Te V/s
不感時間	〜50 %	100 %

§2．実　　験

本実験は、プリアンプのリセット直後に検出したガンマ線イベントに対して、波形解析のアルゴリズム開発とその補正効果の検証を目的として行われた。実験は、10 kHz の陽電子ビームを直接ゲルマニウム検出器に照射し、エネルギー付与率を 0.4 TeV/s (リセット率 2〜3 kHz) としてハイパー核実験の状況を再現したうえで、^{60}Co 線源からのガンマ線を測定した。測定に用いた ^{60}Co 線源はプラスチックシンチレータ (＋光電子増倍管) の中に埋め込まれており、ゲルマニウム検出器と組み合わせてベータ・ガンマ・コインシデンスをとることで効率よくリセット直後のガンマ線イベントにトリガーをかけてデータ収集することに成功した。また比較のため、整形アンプ出力を 2 つに分けフラッシュADC とパルス波高型 ADC で同時に同じイベントを記録した。

§3．解析と考察

リセット直後の整形アンプ出力のベースライン変動の大きさはイベントごとに異なっていることがフラッシュADC の波形データから分かった。このため、イベントごとにベースライン部分を抜き出し、2 次関数でフィッティングして正しいベースライン位置を見積もった上で波高を読み取る解析方法を考えた。ベースライン部分のみを抜き出すアルゴリズムは、波形データを微分してその微係数がゼロに近くなるところを選択する方式をとっている。第 1 図に解析で得られた ^{60}Co のガンマ線スペクトルを示す。波線で表示されているのはパルス波高型 ADC で測定した場合で、リセット直後のベースライン変動によって正しい波高が読めずピークが広がってしまっているのが確認できる。実線で表示されているのは同じイベントをフラッシュ ADC で測定し、ベースラインの補正を行った場合である。2 つを見比べると、補正によってベースライン変動の影響を改善できていることが分かる。現在の解析では、リセット率が 2 MHz の条件下でゲルマニウム検出器の信号を 3.1 keV(半値幅 @ 1 MeV) のエネルギー分解能で読み出すことができている。パルス波高型 ADC ではエネルギー分解能は 3.7 KeV であり、補正によってエネルギー分解能は改善している。また、相対検出効率をピークの面積比で見積もると、パルス波高型 ADC を使った場合にくらべてフラッシュ ADC を使った読み出しの方がリセット直後のイベントに対して約 1.5 倍に増えていることが分かった。以上の結果より、旧 Hyperball 用の読み出し方法では正しく読み出せなかった プリアンプ・リセット直後の

---

*プリアンプ出力を直接読み出すのに必要なフラッシュADC の性能を見積もるとダイナミックレンジが 10 V、有効ビット数が 19 ビット、サンプリング周期が 100 MHz となる。

イベントに対してフラッシュADC を用いた読み出し方法ではオフライン解析で補正することで正しく読み出せることが分かり、波形読み出しの有効性を示すことができたといえる。

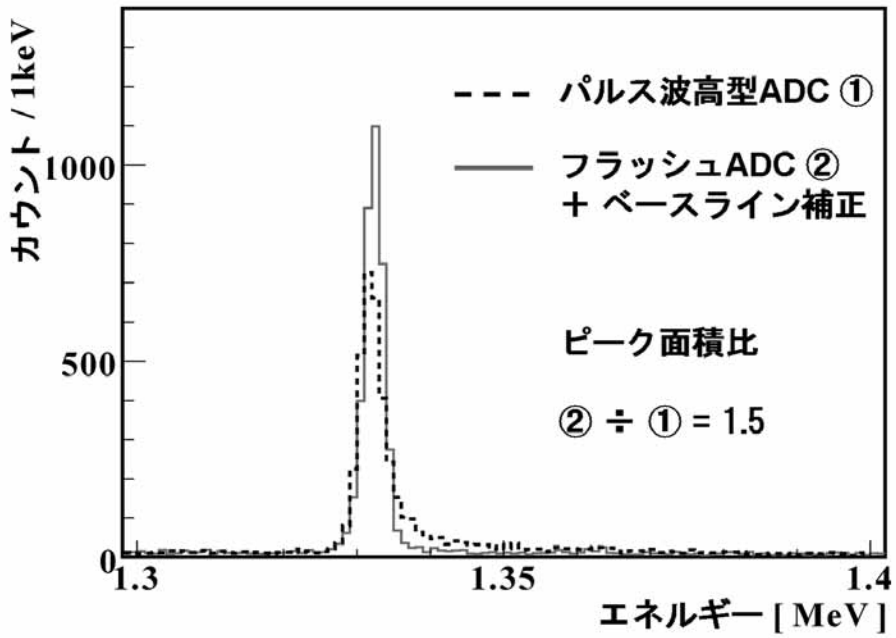

第 1 図　プリアンプ・リセット直後のベースラインが変動しているイベントに対してパルス波高型 ADC とフラッシュADC ＋波形解析で読み出した ^{60}Co 1.33MeV ピークのエネルギースペクトルの比較。

§4．まとめと今後の課題

ゲルマニウム検出器のプリアンプ・リセット直後のベースラインが変動している間に計測されたガンマ線イベントに対してフラッシュADC を使った波形読み出しを行い、得られたデータを元に補正用のアルゴリズムを開発した。オフラインでベースラインのフィッティング解析を行った結果、ベースラインが変動していても補正することで 3.1 keV(半値幅 @ 1 MeV) エネルギー情報を読み出すことに成功した。今後の課題は、開発したベースライン補正アルゴリズムの再検討とパイルアップに対する解析アルゴリズムの開発である。

参　考　文　献

[1] H. Tamura *et al.*: J-PARC proposal E13, ”Gamma-ray spectroscopy of light hypernuclei” (2006).

Ⅱ. Radiochemistry

(LNS Experiment : #2574, #2585)

3種ユークライト隕石（Dhofar 007，Juvinas，Stannern）の希ガスおよび全岩化学組成に関する研究

竹田光世, 大浦泰嗣, 海老原充

首都大学東京大学院理工学研究科 （192-0397 東京都八王子市南大沢 1-1）

Noble Gas and Bulk Chemistry Study of Three Eucrites Juvinas, Stannern and Dhofar 007

M. Takeda , Y. Oura , and M. Ebihara

Graduate School of Science and Engineering, Tokyo Metropolitan University, 1-1 Minami-Ohsawa, Hachioji, Tokyo 192-0372

We performed bulk chemical and noble gas analyses of three eucrite meteorites, Juvinas, Stannern and Dhofar 007 (Dho 007) for their single specimens and estimated ^{244}Pu-Xe age. Juvinas and Stannern are brecciated noncumulate eucrites. Dho 007 is an anomalous cumulate eucrite, which is suggested to be a possible relationship with mesosiderites. We present here new data of bulk chemical composition and chronological information for Dho 007 in addition to these for the other eucrites, Juvinas and Stannern.

§1．はじめに

ユークライト隕石は小惑星の地殻由来の物質であると考えられている隕石である。ユークライト隕石母天体である小惑星は火成活動を経て分化したと考えられており、この小惑星由来の隕石の分析は，惑星進化過程の解明に繋がると考えられている．隕石の初期進化過程を推測する方法の一つとして、放射性核種を利用した年代測定法が挙げられる。中でも、消滅核種（太陽系の年齢〜45.6 億年と比較して短い半減期を持つため現在は存在しない核種）^{244}Pu（半減期〜8100 万年）とその自発核分裂片である Xe を利用した ^{244}Pu-Xe 相対年代法はユークライト隕石の初期形成過程を考察する上で非常に有力な手段である。

1999 年にオマーン砂漠で発見された Dhofar 007（Dho 007）はその鉱物および化学組成は集積岩ユークライトの範囲に入るが、金属片を含み Yamaguchi *et al.* [1] によってユークライトとは異なる隕石グループの一つであるメソシデライトとの関連性が示唆された隕石である。これまでにこの Dho 007 に関しての形成年代は得られていない。そこで本研究では Dho 007 および、非集積岩ユークライトである Juvinas、Stannern について化学組成と希ガス同位体組成を求め、この隕石の Angra dos Reis（^{207}Pb-^{206}Pb 年代 4.5578±0.0004）[2]に対する ^{244}Pu-Xe 相対年代を算出することを試みた。

§2．実　験

東京大学地殻化学実験施設より提供された3つのユークライト隕石（Juvinas, Stannern, Dho 007）を試料として用いた。試料はそれぞれ希ガス同位体分析用（125〜190 mg）と全岩化学組成分析用（180〜265 mg）の二つに分け、希ガス同位体分析は東京大学地殻化学実験施設の希ガス質量分析装置（VG-5400、MS-II）を用いて行った。全岩化学組成は即発γ線分析（PGA）、機器中性子放射化分析（INAA）、機器光量子放射化分析（IPAA）の3種の放射化分析法により求めた。さらに，ここでは詳細を省略するがBa、希土類元素、Th、U濃度を誘導結合プラズマ質量分析により求めた。放射化分析の概略を以下に示す。

PGA：全岩化学分析用の試料（粗粒状）の全量を四フッ化エチレン六フッ化プロピレンフィルム封入し、日本原子力研究開発機構（JAEA）JRR-3M実験ホール内の即発γ線分析装置にて約3時間、中性子照射・測定を行った。

INAA：PGA後の試料をメノウ乳鉢で粉末化し、一部（20から30 mg）を高純度ポリエチレンフィルムに封入した。これらの試料に対し、JAEAのJRR-3、PN-3にて10秒間中性子照射を行い、その後速やかにγ線を測定した。またこの試料を約2ヶ月冷却し、JAEAのJRR-4、T-pipeにて20分間中性子照射した後、適当な冷却時間を置いて、首都大学東京RI研究施設にてγ線測定を複数回行った。

IPAA：PGA後粉末化した試料の一部（約30 mg）をAl箔に包み、直径10 mmの円板状に整形した。比較標準試料である岩石標準試料JB-1、Allende隕石も同様に調整した。これをフラックス補正の為の金箔と共に石英管に常圧封入し、東北大学原子核理学研究施設電子線形加速器にて最大エネルギー30 MeVの制動放射で30分間照射し、ただちにγ線測定を行った。更に測定後の試料を約4時間半照射し、適当な冷却時間を置いて、首都大学東京RI研究施設にてγ線測定を複数回行った。

§3．結果と考察

3つの放射化分析の組み合わせにより主要・微量元素が、またICP-MSによりBa、希土類元素、Th、Uが定量できた。放射化分析による定量結果を第1表にまとめた。Juvinas、Stannernではすべての元素で、Kitts and Lodders (1998) [3]の編纂値の範囲に入った。しかしDho 007では、得られた結果がYamaguchi *et al.*. (2006) の値と大きく異なり、特に希土類元素では文献値の2〜3倍の濃度を示し、希土類元素存在度パターンも異なる傾向を示した。Dho 007は発見された総量がおよそ21 kgと大きく、Yamaguchi *et al.* (2006) とは試料の提供源が異なる。このことから、Dho 007の組成の違いは隕石の部位の違いによる不均一が原因であると考えられるが、本研究では鉱物学的観察等は行っておらず、今後の課題である。

計算法の詳細は省略するが、この結果と希ガス同位体分析の結果を用いて^{244}Pu-Xe相対年代を算出したところ、Juvinas（-24±5 Ma）、Stannern（-103±30 Ma）については文献値（Juvinas：-10±23 Ma、Stannern：-124±13 Ma）[4]と良く一致する年代が得られたが、Dho 007では年代値として妥当な値を得ることができなかった。この原因として、Dho 007が地球上での風化を受けている可能性が挙げられる。^{244}Pu-Xe相対年代を求めるには隕石のBa、軽希土類元素（LREE；La + Ce + Nd）の比とUの含有量が必要である [3]。しかしDho 007は砂漠隕石であり、これらの元素濃度が地球上での風化の影響により本来の濃度から変化した可能性があるので、これを考慮して年代を算出する必要がある。横軸にYb、縦軸にSrやBaなどの風化の影響を受けやすい元素をとって文献値 [5, 6]と共にプロットすると、Dho 007は他のユークライト隕石で見られる元素の相関から明らかに外れたところにプロットされる（第1図）。これよ

第 1 表　即発 γ 線分析、機器中性子放射化分析、機器光量子放射化分析によるユークライト隕石の定量結果。

		Juvinas		Stannern		Dhofar007	
		this work	lit.*	this work	lit.*	this work	lit. **
Si	%	22.6 ± 0.5	22.97 ± 0.3	23.3 ± 0.5	23.00 ± 0.45	22.9 ± 0.5	21.6
Ti	%	0.437 ± 0.001	0.3713 ± 0.0231	0.576 ± 0.001	0.586 ± 0.0272	0.219 ± 0.001	0.123
Al	%	6.87 ± 0.06	6.93 ± 0.20	6.20 ± 0.04	6.47 ± 0.37	5.80 ± 0.04	6.67
Cr	ppm	1940 ± 3	1783 ± 369	2119 ± 3	2081 ± 330	2854 ± 5	3052
Fe	%	14.48 ± 0.04	13.9 ± 0.9	14.7 ± 0.0	14.1 ± 1.0	13.3 ± 0.0	12.2
Mn	%	0.435 ± 0.010	0.404 ± 0.020	0.434 ± 0.011	0.392 ± 0.361	0.409 ± 0.010	0.403
Mg	%	3.89 ± 0.33	4.22 ± 0.10	4.28 ± 0.40	4.23 ± 0.24	6.61 ± 0.49	5.67
Ca	%	6.50 ± 0.02	7.66 ± 0.40	6.89 ± 0.02	7.54 ± 0.31	5.95 ± 0.02	8.22
Na	%	0.300 ± 0.001	0.320 ± 0.028	0.412 ± 0.001	0.403 ± 0.046	0.278 ± 0.001	0.257
K	%	0.026 ± 0.005	0.0328 ± 0.0064	0.062 ± 0.008	0.0646 ± 0.0078	0.033 ± 0.005	0.0241
B	ppm	0.90 ± 0.11	0.965 ± 0.474	1.17 ± 0.14	3.390 ± 3.361	0.987 ± 0.136	
S	%	0.705 ± 0.044	0.15 ± 0.10	0.52 ± 0.05	0.19 ± 0.12	2.76 ± 0.07	0.465
Cl	ppm	n. d.	28.50 ± 14.80	n. d.	34.5	305 ± 19	
V	ppm	59.3 ± 3.8	85 ± 16	54.5 ± 3.7	77.0 ± 12.0	86.9 ± 4.0	81.6
Sc	ppm	31.13 ± 0.07	28 ± 1.6	31.05 ± 0.08	31.2 ± 0.85	24.81 ± 0.06	21.61
Co	ppm	6.58 ± 0.08	4.7 ± 0.9	4.89 ± 0.07	6.6 ± 3.4	50.5 ± 0.2	59.8
Ni	%	n. d.	4 ± 3.4	n. d.	7 ± 2.8	0.115 ± 0.001	0.0929
Sr	ppm	70.2 ± 3.0	74.9 ± 5.2	88.0 ± 1.3	88.8 ± 6.0	127 ± 2	
Y	ppm	19.5 ± 0.7	16.5 ± 0.7	30.3 ± 1.0	27 ± 1.2	8.06 ± 0.48	
Zr	ppm	45.1 ± 0.7	44.9 ± 1.6	93.8 ± 0.9	88 ± 1.1	21.03 ± 0.53	
La	ppm	2.95 ± 0.04	2.582 ± 0.238	5.13 ± 0.06	5.166 ± 0.320	1.14 ± 0.03	0.386
Ce	ppm	8.92 ± 0.45	6.934 ± 0.563	13.9 ± 0.6	13.344 ± 0.694	2.21 ± 0.49	0.908
Sm	ppm	1.90 ± 0.01	1.623 ± 0.128	3.13 ± 0.01	3.227 ± 0.175	0.632 ± 0.006	0.261
Eu	ppm	0.71 ± 0.05	0.624 ± 0.036	0.84 ± 0.07	0.808 ± 0.047	0.420 ± 0.022	0.330
Yb	ppm	1.88 ± 0.07	1.602 ± 0.188	2.96 ± 0.10	2.663 ± 0.314	0.899 ± 0.046	0.427
Lu	ppm	0.27 ± 0.01	0.255 ± 0.024	0.41 ± 0.02	0.408 ± 0.028	0.128 ± 0.009	0.067
Ir	ppb	n. d.	0.096 ± 0.08	n. d.	0.12 ± 0.01	54.9 ± 1.4	49
Au	ppb	n. d.	4.3 ± 3.4	n. d.	6.85 ± 9.43	19.9 ± 1.2	9.2

*Kitts and Lodders (1998). **Yamaguchi *et al.* (2006).

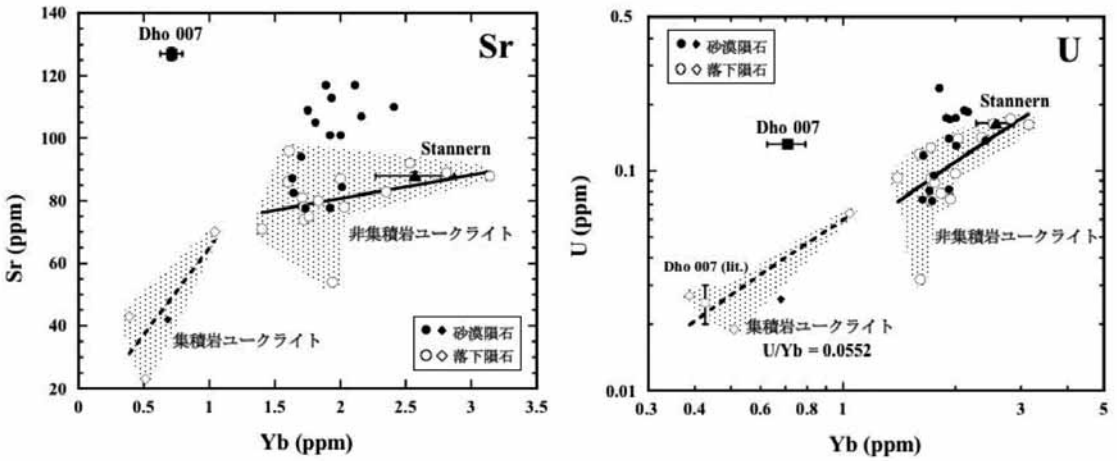

第 1 図　集積岩ユークライト、非集積岩ユークライトにおける元素濃度の相関。影の部分は砂漠隕石を除いた隕石の取る値の範囲を、破線および実線はそれぞれ集積岩ユークライト、非集積岩ユークライトに対する回帰曲線を示す。(a)Yb 濃度と Sr 濃度の相関。(b)Yb 濃度と U 濃度の相関。

り、Dho 007 では Sr、Ba、LREE、U で風化の影響を受けていることが判った。さらに，Yamaguchi *et al.* (2006) の値からも外れた所にプロットされていることが分かる。これは前述の通り試料部位の差によると考えられ、隕石の部位によって風化の度合いも異なることを示している。以上から、U 含有量は第 1 図 (b) の U/Yb から、また Ba/LREE は Ba と LREE の相関（第 2 図）から見積もった値を用い、Dho 007 の ^{244}Pu-Xe 相対年代を算出したところ、-10±2 Ma という値を得ることができた。

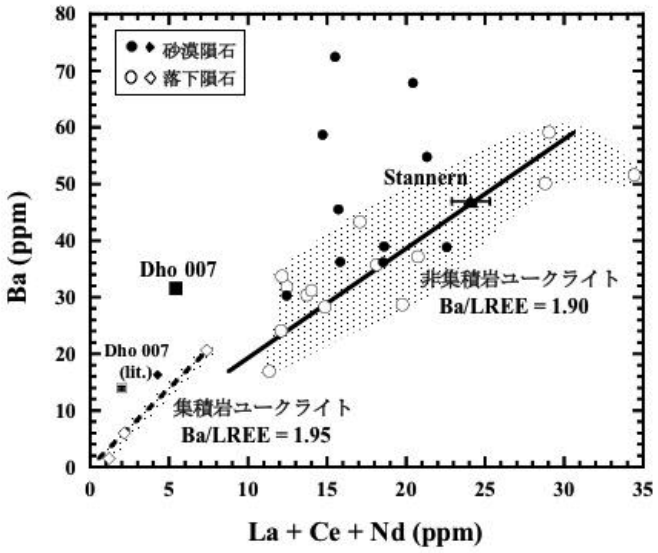

第 2 図　第 2 図 集積岩ユークライト、非集積岩ユークライトにおける Ba と LREE（La + Ce + Nd）の相関。影および破線、実線の示すものは第 1 図に同じ。

他のユークライト隕石の年代 [3] と比較した結果、この隕石がユークライト隕石の中でも、かなり古い年代を示すことが判った。この Dho 007 については今後用いた部位について鉱物学的観察を行い、その結果と合わせてこの年代値の意味を考える必要がある。

§4. ま と め

特異な集積岩ユークライトである Dho 007 を含めた 3 つのユークライト隕石について、放射化分析と質量分析により、希ガス同位体組成、全岩化学組成を求めた。この結果からこれら 3 つの隕石について ^{244}Pu-Xe 相対年代を算出した。Dho 007 では風化の影響を考慮して年代を得たが、この結果からこの隕石がユークライト隕石の中で、かなり古い年代を持つものであることが判った。

謝辞

本研究を行うにあたり良質な電子ビームを供給していただいた東北大学原子核理学研究施設マシングループの方々と、試料照射ならびに放射線測定でお世話になった大槻勤准教授と結城秀行博士に深く感謝する。

参　　考　　文　　献

[1] Yamaguchi *et al.*: Meteorit. Planet. Sci. **41** (2006) 863.

[2] Lugmair and Galer: Geochim. Cosmochim. Acta **56** (1992) 1673.

[3] Kitts and Lodders: Meteorit. Planet. Sci. **33 (Suppl.)** (2000) A197.

[4] Miura *et al.*: Geochim. Cosmochim. Acta **62** (1998) 2369.

[5] Barrat *et al.*: Meteorit. Planet. Sci. **35** (2000) 1087.

[6] Barrat *et al.*: Geochim. Cosmochim. Acta **67** (2003) 3959.

Ⅲ. List of Publication

List of Publication（論文リスト）（2006.1～2006.12）

Papers Published in Refereed Journals

Photoproduction of η-mesons off C and Cu Nuclei for Photon Energies below 1.1 GeV.

T. Kinoshita, H. Yamazaki, H. Fukasawa, K. Hirota, 1, T. Ishikawa, J. Kasagi, A. Kato, T. Katsuyama, K. Kino. Miyahara, T. Nakabayashi, K. Nawa, K. Okamura, Y. Saitoh, K. Satou, M. Sengoku, H. Shimizu, K. Suzuki, S. Suzuki, T. Terasawa, H. Kanda, K. Maeda, T. Takahashi, Y. Aruga, T. Fujinoya, A. Iijima, M. Itaya, Y. Ito, T. Iwata, H. Kato, T. Kawamura, T. Michigami, M. Moriya, T. Sasaki, Y. Tajima, S. Takita, T. Noma, M. Yamamoto, H.Y. Yoshida, Y. Yoshida, O. Konno, T. Maruyama and T. Yorita

Phys. Lett. **B639** (2006) 429 -435.

Photoproduction of ηMesons off Protons for $E_\gamma \leqq 1.15$ GeV.

T. Nakabayashi, H. Fukasawa, R. Hashimoto, T. Ishikawa, T. Iwata, H. Kanda, J. Kasagi, T. Kinoshita, K. Maeda, F. Miyahara, K. Nawa, T. Nomura, Shimizu, T. Shishido, K. Suzuki, Y. Tajima, T. Takahashi, H. Ueno, H. Yamazaki, and H.Y. Yoshida

Phys. Rev. **C74** (2006) 035202 (1-7).

Photo-Production of Neutral Kaons on C-12 in the Threshold Region.

T. Watanabe, P. Bydžovský, K. Dobashi, S. Endo, Y. Fujii, O. Hashimoto, T. Ishikawa, K. Itoh, H. Kanda, M. Katoh, T. Kinoshita, O. Konno, K. Maeda, A. Matsumura, F. Miyahara, H. Miyase, T. Miyoshi, K. Mizunuma, Y. Miura, S.N. Nakamura, H. Nomura, Y. Okayasu, T. Osaka, M. Oyamada, A. Sasaki, T. Satoh, H. Shimizu, M. Sotona, T. Takahashi, T. Tamae, H. Tamura, T. Terasawa, H. Tsubota, K. Tsukada, M. Ukai, M. Wakamatsu, H. Yamauchi and H. Yamazaki

Physics Letters **B651** (2007) 269-274.

Measurement of E2-E0 Strength in the Isovector Giant Resonance (GQR-GMR) Region of ^{28}Si Nuclei through the (e, e'n) Reaction.

K. Kino, T. Saito, T. Nakagawa, T. Tamae, I. Nishikawa, Y. Asano, H. Toda, M. Watabe, T. Nakagawa, H. Tsubota, K. Takahashi, M. Utoyama, M. Higuchi, Y. Matsuura, H. Ueno, and T. Suzuki

Phys. Rev. **C73** (2006) 034614 (1-6).

Isovector Quadrupole Resonance in ^{13}C(γ, n) Reaction.

K. Maeda, S. Ito, H. Itoh, O. Konno, H. Matsuyama, T. Murakami, T. Sasaki, T. Suda, M. Takeya, and T. Terasawa

J. Phys. Soc. Japan **75** (2006) 034201 (1-8).

200-MeV Bremsstrahlung Tagged Photon Beams at Sendai.

K. Hirose, M. Chiba, M. Inoue, H. Kanda, R. Kimura, K. Kino, Y. Kobayashi, O. Konnno, K. Maeda, H. Miyase, A. Miyamoto, T. Otsuki, A. Saito, T. Suda, K. Takahashi, T. Tamae, Y. Terasaki, T. Terasawa, H. Tsubota, T. Tsuruta, M. Utoyama, H. Yuuki, Y. Yamaguchi,

and H. Yamazaki

Nucl. Instrm. and Meth. **A564** (2006) 100-107.

Differential Cross Section and Photon-Beam Asymmetry for the $\vec{\gamma} n \rightarrow K^+ \Sigma$ Reaction at E_γ = 1.5 - 2.4 GeV.

H. Kohri, D.S. Ahn, J.K. Ahn, H. Akimune, Y. Asano, W.C. Chang, S. Date', H. Ejiri, S. Fukui, H. Fujimura, M. Fujiwara, S. Hasegawa, K. Hicks, T. Hotta, K. Imai, T. Ishikawa, T. Iwata, H. Kawai, Z.Y. Kim, K. Kino, N. Kumagai, S. Makino, T. Mart, T. Matsuda, T. Matsumura, N. Matsuoka, T. Mibe, M. Miyabe, Y. Miyachi, M. Morita, N. Muramatsu, T. Nakano, M. Niiyama, M. Nomachi, Y. Ohashi, H. Ohkuma, T. Ooba, D.S. Oshuev, C. Rangacharyulu, A. Sakaguchi, T. Sasaki, P.M. Shagin, Y. Shiino, A. Shimizu, H. Shimizu, Y. Sugaya, M. Sumihama, Y. Toi, H. Toyokawa, A. Wakai, C.W. Wang, S.C. Wang, K. Yonehara, T. Yorita, M. Yoshimura, M. Yosoi, and R.G.T. Zegers

Phys. Rev. Lett. **97** (2006) 082003 (1-5).

The $\vec{\gamma} p \rightarrow K^+ \Lambda$ and $\vec{\gamma} p \rightarrow K^+ \Sigma^0$ Reactions at Forward Angles with Photon Energies from 1.5 to 2.4 GeV.

M. Sumihama, J.K. Ahn, H. Akimune, Y. Asano, C. Bennhold, W.C. Chang, T. Corthals, S. Date, H. Ejiri, H. Fujimura, M. Fujiwara, M. Guidal, K. Hicks, T. Hotta, K. Imai, T. Ishikawa, T. Iwata, H. Kawai, Z.Y. Kim, K. Kino, H. Kohri, N. Kumagai, S. Makino, T. Mart, T. Matsumura, N. Matsuoka, T. Mibe, M. Miyabe, Y. Miyachi, M. Morita, N. Muramatsu, T. Nakano, M. Niiyama, M. Nomachi, Y. Ohashi, T. Ooba, H. Ohkuma, D.S. Oshuev, C. Rangacharyulu, A. Sakaguchi, T. Sasaki, P.M. Shagin, Y. Shiino, H. Shimizu, Y. Sugaya, H. Toyokawa, A. Wakai, C.W. Wang, S.C. Wang, K. Yonehara, T. Yorita, M. Yosoi, and R.G.T. Zegers

Phys. Rev. **C 73** (2006) 035214 (1-12).

Measurements of the Generalized Electric and Magnetic Polarizabilities of the Proton at Low Q^2 Using the Virtual-Compton-Scattering Reaction.

P. Bourgeois, Y. Sato, J. Shaw, R. Alarcon, A. M. Bernstein, W. Bertozzi, T. Botto, J. Calarco, F. Casagrande, M. O. Distler, K. Dow, M. Farkondeh, S. Georgakopoulos, S. Gilad, R. Hicks, M. Holtrop, A. Hotta, X. Jiang, A. Karabarbounis, J. Kirkpatrick, S. Kowalski, R. Milner, R. Miskimen, I. Nakagawa, C. N. Papanicolas, A. J. Sarty, S. Sirca, E. Six, N. F. Sparveris, S. Stave, E. Stiliaris, T. Tamae, G. Tsentalovich, C. Tschalaer, W. Turchinetz, Z.-L. Zhou, and T. Zwart

Phys. Rev. Lett. **97** (2006) 212001 (1-4).

Measurement of Evaporation Residue Cross-Section of the Reaction $^{30}Si + ^{238}U$ at Subbarrier Energies.

K. Nishio, S. Hofmann, F.P. Hessberger, D. Achermann, S. Antalic, V.F. Comas, Z. Gan, S. Heinz, J.A. Heredia, H. Ikezoe, J. Khuyagbaatar, B. Kindler, I. Kojouharov, P. Kuusiniemi, B. Lommel, R. Mann, M. Mazzocco, S. Mitsuoka, T. Ohtsuki, A.G. Popeko, S. Saro, H.J. Schott, B. Sulignano, A. Svirikhin, K. Tsuruta, and A.V. Yeremin

Europian Physical Journal **A 29** (2006) 281-287.

Status of the Electron Accelerator for Radioanalytical Studies at Tohoku University.

T. Ohtsuki, H. Yuki, K. Hirose, and T. Mitsugashira

Czech Journal of Physics **56** (2006) D391-398.

Radiochemical Studies at the Cyclotron Laboratory Tohoku University.

T.Ohtsuki, K. Shikano, H. Yuki, K. Hirose, and K. Takamiya

Czech Journal of Physics **56** (2006) D425-432.

Conceptual Design of an Isochronous Ring to Generate Coherent Terahertz Synchrotron Radiation.

H. Hama, H. Tanaka, N. Kumagai, M. Kawai, F. Hinode, T. Muto, K. Nanbu, T. Tanaka, K. Kasamsook, K. Akiyama, and M. Yasuda

New J. Phys. **8** (2006) 292.

Papers Published in International Conference Proceedings

Low-Energy Li+D Reactions with Li Target in Various Phases.

H. Yonemura, J. Kasagi, M. Honmo, Y. Ishikawa, T. Wang and Y. Zhang

Proceeings of International Conference on Reaction Mechanism and Nuclear Structure at the Coulomb Barrier, AIP Conference Proceedings **853** (2006) 372-377.

Super Coherent THz Light Source Based on an Isochronous Ring with Very Short Electron Bunches.

H. Hama, K. Akiyama, F. Hinode, K. Kasamsook, M. Kawai, T. Muto, K. Nanbu, T. Tanaka, M. Yasuda, and H. Tanaka

Proceedings of the 28th International Free Electron Laser Conference, FEL2006, Berlin, Germany (2006) 371-374.

A Compact Low Emittance DC Gun Employing Single Crystal Cathode of LaB6.

K. Kasamsook, K. Akiyama, H. Hama, F. Hinode, M. Kawai, T. Muto, K. Nanbu, T. Tanaka, and M. Yasuda

Proceedings of the 28th International Free Electron Laser Conference,

FEL2006, Berlin, Germany (2006) 680-683.

Ⅳ. Approved Experiments

平成18年度前期採択課題一覧表

課題番号	課　　題　　名	申込責任者	採　択 シフト数
原子核関連分野			
2563	検出器テスト用電子ビームラインの整備	清水　　肇	8
2564	e^+e^- 対生成によるSTB-Tagger Ⅱ のエネルギー較正	石川　貴嗣	15
2565	Photoproduction of Neutral Kaons on Deuterium Target near Threshold Region	橋本　　治	120
2566	指向性をもった電子検出器の性能評価	友野　　大	12
2567	Letter of Intent NKS2でのΛ粒子検出器のテスト －生成閾値エネルギーでの $\gamma d \rightarrow \Theta^+$ 反応の研究－	石川　貴嗣	
加速器関連分野			
2568	Cure of longitudinal Coupled-Bunch Instability on the STB Ring	浜　　広幸	10
放射化学・物性関連分野			
2569	標識化による金属内包フラーレン及びヘテロフラーレンの製造及びその応用研究	大槻　　勤	2
2570	水素誘起空孔による拡散の促進	山崎　仁丈	2
2571	光核分裂反応断面積の実測値と計算値の比較	中西　　孝	2
2572	光量子放射化分析法による光通信用材料中の不純物評価	鹿野　弘二	1
2573	金属材料等中の軽元素の分離・捕集法の開発と定量	桝本　和義	2
2574	宇宙化学的試料および環境試料の光量子放射化分析	大浦　泰嗣	2
2575	固体抽出剤を用いた希土類元素とアクチノイド元素の分離に関する研究	鈴木　達也	2

平成18年度後期採択課題一覧表

課題番号	課　　題　　名	申込責任者	採　択 シフト数
原子核関連分野			
2576	水素・重水素標的における π^0、 η 光生成反応	清水　　肇	38
2577	電子ビームによる大型BSO単結晶の特性試験	清水　　肇	3
2578	中性K中間子スペクトロメータ NKS2 での電子・陽電子除去のためのシリカエアロジェルチェレンコフ検出器の開発	石川　貴嗣	1
2579	鉛シンチレーティングファイバー検出器のエネルギー応答性	石川　貴嗣	4
2580	RHIC PHENIX 実験における高運動量ミューオントリガーのためのカソードストリップチェンバー読み出し回路の性能評価	齊藤　直人	8
2581	窒化ガリウム検出器の放射線耐性の測定	成田　晋也	2
放射化学・物性関連分野			
2582	標識化による金属内包フラーレン及びヘテロフラーレンの製造及びその応用研究	大槻　　勤	2
2583	光核分裂反応断面積の実測値と計算値の比較	中西　　孝	2
2584	光量子放射化分析法による光通信用材料中の不純物評価	鹿野　弘二	1
2585	宇宙化学的試料および環境試料の光量子放射化分析	大浦　泰嗣	2
2586	固体抽出剤を用いた希土類元素とアクチノイド元素の分離に関する研究	鈴木　達也	2
随時申込			
2587	J-PARC 実験用 Ge 検出器の Readout System の開発	田村　裕和	1

核理研研究報告　第40巻

2008年3月発行

発行所　東北大学大学院理学研究科
附属原子核理学研究施設
仙台市太白区三神峯1-2-1（郵便番号982－0826）
電話　022－743－3400

印刷所　株式会社　東北プリント
仙台市青葉区立町24番24号
TEL　022（263）1166㈹

RESEARCH REPORT OF
LABORATORY OF NUCLEAR SCIENCE
TOHOKU UNIVERSITY

Volume 40 March 2008

Laboratory of Nuclear Science, Tohoku University,
1-2-1, Mikamine, Taihaku, Sendai 982-0826, Japan

東北大学大学院理学研究科
原 子 核 理 学 研 究 施 設